Impact assessment of legacy wastes from ancient mining activities on current earthworm community

Anne-Lise Mariet, Honorine Gauthier-Manuel, Tiffany Lagiewski, Carole Bégeot, Anne-Véronique Walter-Simonnet, Frédéric Gimbert

HAL Id: hal-02930050
https://hal.inrae.fr/hal-02930050

Submitted on 22 Aug 2022

1 **Impact assessment of legacy wastes from ancient mining activities on current earthworm**

2 **community**

3 Anne-Lise Mariet, Honorine Gauthier-Manuel, Tiffany Lagiewski, Carole Bégeot, Anne-

4 Véronique Walter-Simonnet, Frédéric Gimbert*

5

6 *Department of Chrono-Environment, University of Bourgogne Franche-Comté, UMR*

7 *UFC/CNRS 6249 USC INRA, 16 route de Gray, F-25030 Besançon Cedex, France*

8

9

10

11

12

13

14

15 *Corresponding author:

16 Frédéric Gimbert

17 Tel.: +33 (0) 381 665 775

18 Fax: +33 (0) 381 665 797

19 E-mail address: frederic.gimbert@univ-fcomte.fr

Abstract

Mineral resource exploitation by human societies throughout history led to the deposit of mining and smelting wastes and the subsequent contamination of surrounding soils by trace metals. After several centuries, the impact of these legacy hazardous wastes may remain a cause of environmental concern, especially for indigenous soil invertebrate populations such as earthworms. Therefore, we conducted a passive biomonitoring campaign in a former metallurgical district (Vosges Mountains, eastern France). According to community descriptors, we evidenced a significant decrease of anecic and endogeic earthworm density in the former mining stations. To link these results to soil contamination and bioaccumulation levels in earthworm tissues, we propose an original modelling approach using nonlinear mixed-effects regression models. Beyond a dose-response relationship between metal internal concentrations and their levels in soils, we highlighted contrasted behaviors according to ecological groups (epianecics and endogeics most impacted). We interpreted these results in relation to some eco-physiological features without completely exclude the influence of textural characteristics of soil, especially for deep-burrowing species such as anecic strict. Nonetheless, the presence of earthworm populations currently living in highly contaminated sites and handling elevated internal concentrations raises the question of the acquisition of genetic adaptive traits and the trophic transfers of metals.

1- Introduction

Throughout history, mining and smelting activities of metals such as iron (Fe), copper (Cu), lead (Pb), or silver (Ag) have played a leading role in the socio-economic development of human societies (Tylecote, 1987). However, at the same time, they generated significant amounts of potentially contaminated wastes whose weathering led to the release of trace metals (TMs) in the environment. In Europe, the former mining district of Sainte-Marie-aux-Mines (Vosges Mountains, eastern France) is known for its metal exploitation over the last millennium and especially Pb and Ag during the 15th-16th centuries (Fluck, 2006). In this particular district, it is estimated that more than 10% of the area is nowadays covered by several types of metallurgical wastes, i.e., ore dumps, slags, and ore-washing sediments (Fluck, 2000; Mariet et al., 2014). Persisting just a few centimeters deep, they affect both the physical (structure, texture) and chemical properties of current soils. For instance, the contamination by TMs is very elevated (up to several tens of thousands of mg_{Pb} kg^{-1} soil) and still highly available for potential transfers (Mariet et al., 2017b). Hence, using an active biomonitoring approach with the land snail *Cantareus aspersus*, it has been recently demonstrated that TMs from medieval mining activities (Pb-Ag extraction) were still bioavailable for this soil invertebrate (Mariet et al., 2016) and represent a risk for environmental health (Mariet et al., 2017a). But what about the current impacts of this legacy contaminated wastes on invertebrate populations living locally on these sites? To answer this question, we conducted a passive bioindication campaign in the former mining district of Sainte-Marie-aux-Mines by sampling earthworms at forested stations subjected to different mining operations and presenting a contamination gradient.

As key organisms of soil functioning, earthworms are well recognized as good indicators of environmental quality since they respond to a variety of environmental and ecological factors such as changes in soil use and contamination (Pérès et al., 2011; Tondoh et al., 2007). Moreover, although abundance is a classical endpoint for the assessment of

67 earthworm community responses to environmental stress, ecological structure (i.e., the

68 proportion of three main morpho-ecological groups: epigeic, endogeic and anecic) seems to be

69 a more sensitive indicator of soil pollution. Indeed, Pérès et al. (2011) showed that soil

70 contamination by PAHs and metals in industrial wastelands did not lead to a modification of

71 earthworm abundance although the ecological structure was strongly impacted. In the same

72 line, Nahmani et al. (2003) found, in soils from a former zinc smelter complex, a global

73 reduction of earthworm densities in relation with an eradication of endogeic species and a

74 reduction of epigeics.

75   The objectives of this study were, therefore, to assess the responses of the current

76 earthworm community to past mining activities dating from several centuries ago and for which

77 only scarce data are available in the literature. The impact on the community will be assessed

78 by various community descriptors, as the density and ecological group distribution of

79 earthworms, and originally completed by statistical consideration of bioaccumulation levels of

80 several TMs in earthworm tissues belonging to different morpho-ecological categories.

81

82   **2- Material and methods**

83   **2-1- Study sites**

84   The study site is located in the former mining district of Sainte-Marie-aux-Mines

85 (Vosges Mountains, France). Four forested stations (100 m²), called MA5, CF20, CF28, and

86 CF29, were chosen according to their soil TM concentrations (Table 1) and to the presence of

87 various types of mining wastes: ore dump on CF28, ore-washing sediments on CF29, and

88 tailings from ancient mining wells on CF20. Lastly, according to the low TM concentrations

89 measured in soils, station MA5 constitutes the control station. The habitat descriptors, in terms

90   of dominating tree species and main physicochemical characteristics, are presented in Table 2.

91   More details are also available in Mariet et al. (2016).

92   **2-2- Sampling procedures and earthworm determination**

93   For each station, sampling of autochthonous earthworms was carried out in spring

94   (April) following the mustard method (Singh et al., 2016). Two spreadings (10 L each) of

95   freshly diluted mustard (15 g L^{-1}) were applied, with an interval of 15 minutes, on a triplicate

96   surface of 1 m² representative of the entire station. Then, the earthworm sampling was

97   completed by hand sorting up to 30 cm depth (Pelosi et al., 2009). Sampled animals were rinsed

98   and sorted by ecological groups (Bouché, 1977): epigeics, endogeics, epianecics, and anecic

99   strict. The earthworms were left to empty their guts for 48 hours in moistened Petri dishes,

100 individually weighted, pooled by ecological groups, and sacrificed at -80°C. For each station

101 and ecological group, some individuals were stored in 95% alcohol for identification at the

102 species level, when possible, using Bouché's key (1972).

103   Soils were also sampled at each sampling plot at three depths of the soil profile: 0-5 cm,

104 5-15 cm, and 15-30 cm. They were sieved to 2 mm, dried at 30°C, and stored for further TM

105 analyses. According to their ecological niche, ecological groups were associated with particular

106 soil depths: 0-5 cm for epigeic earthworms, 15-30 cm for endogeic earthworms, and 0-30 cm

107 for anecic earthworms.

108   **2-3- Trace metal analyses**

109   The total concentrations of Ag, arsenic (As), cadmium (Cd), cobalt (Co), and Pb in soils

110 (Table 1) were measured on dried samples after hot *aqua regia* digestion (HNO_3:HCl, 2:5, v/v)

111 by ICP-MS (Thermo X2 Series) at the Chrono-Environment Laboratory. These five metals were

112 chosen according to their significant contents in exploited ores and identified as anomalous

113 elements in soils (Mariet et al., 2016). The analytical precision and accuracy were checked

114   using a standard reference material (SRM) (Sigma Aldrich CRM052 Loamy Clay 1) with

115   recovery rates of 97 ± 4 %, on average for all TMs.

116   Earthworms were freeze-dried, ground, and digested in HNO_3 by hot mineralization

117   before ICP-MS analyses (Thermo X2 Series). Analytical precision and accuracy were checked

118   using SRM (TORT-2, Lobster hepatopancreas; National Standard, Ottawa, ON, Canada). The

119   recovery rates were 100 ± 13%, on average, for all TMs.

120   **2-4- Soil physicochemical characteristics**

121   Organic matter (OM) content, pH_{water} and texture (sand, silt, and clay) were determined

122   on soils (0-30 cm) by the Laboratoire d'Analyse des Sols at the Institut National de la Recherche

123   Agronomique (INRA) in Arras (France), which has earned COFRAC (French Accreditation

124   Committee) accreditation n°1-1380 for its analytical quality of soil characteristics (Table 2).

125   **2-5- Statistical analyses**

126   The TM concentrations in soils were compared among both the stations and depths using

127   a Kruskal-Wallis test ($p<0.05$) followed by a post-hoc multiple comparison (pgirmess R

128   package). Difference of distribution of ecological groups between stations has been tested by

129   Chi-square test ($p<0.05$). Then, differences of total density or density of ecological groups

130   between stations were tested using Tukey HSD ($p<0.05$). The same procedure was used to

131   highlight significant differences of biomass (Figure S1).

132   Principal component analysis (PCA) was carried out to assess the co-variation between

133   community descriptors (total density and biomass), soil contamination (total Ag, As, Cd, Co,

134   and Pb concentrations) and soil characteristics as texture (sand and silt contents), pH, and OM

135   content.

136   The relationships between TM concentration in earthworms and soil contamination on

137   the one hand and, on the other hand, earthworm density and TM concentration in earthworms

138   were tested separately using nonlinear mixed-effects regression models (nlme R package),

139   integrating the earthworm ecological group as fixed effect and the sampling plot as random

140   intercept. The following models were used:

141    $$[TMs]_{earthworm} = a * \ln([TMs]_{soil}) + b$$

142    $$density = d0 * \exp(-k * [TMs]_{earthworm})$$

143   For all of the models, when residuals were skewed, variance functions (power and

144   exponential) were applied, and the best model was selected according to Akaike's Information

145   Criterion (pgirmess R package). The effect of ecological group was tested using a likelihood-

146   ratio test (LRT, $p < 0.05$). When a significant relationship was found, pairwise Wald t-tests of

147   the estimated coefficients were carried out between ecological groups by re-ordering treatments

148   in nlme models using the *relevel* R function (stats R package).

149   All of the statistics were performed with R (3.4.0) (R Core Team, 2014).

150

151   **3- Results**

152   **3-1- Earthworm community description**

153   The main representative species of each ecological group are summarized in Table 3.

154   The earthworm communities were quite similar between the stations studied with *Lumbricus*

155   sp. in the epigeic group, *Aporrectodea caliginosa* in the endogeic group, *Lumbricus rubellus* in

156   the epianecic group and *Aporrectodea* sp. in the anecic strict group. An endemic species of the

157   Vosges Mountains, *Allolobophora zicsii* (Bouché, 1972), an endogeic, was sampled in the MA5

158   station (Table 3).

159   The total density of earthworms sampled at each station showed significant differences

160   with average values of 57 ± 26, 41 ± 10, 9 ± 4 and 10 ± 2 ind m⁻² for MA5, CF20, CF29, and

161   CF28, respectively (Fig. 1). The density of epigeic earthworms was not significantly different

162   between each station, comprised between 4 and 6 ind m⁻². For the other ecological categories,

163   the stations can be grouped into two lots based on significant differences of density: on the one

164   hand, MA5 and CF20, and on the other hand, CF29 and CF28 with lower densities of

165   epianecics, anecic strict, and endogeics (Fig. 1). The same pattern was observed for the biomass

166   of earthworms (Figure S1). The highest average density was reached by the anecic strict in

167   MA5 (45 g m⁻²) and CF20 (25 g m⁻²), although their density was the lowest in the stations CF29

168   (0.2 g m⁻²) and CF28 (0 g m⁻²).

169   The multivariate analysis allowed linking the community descriptors with the

170   physicochemical characteristics of the stations (Fig. 2). The first axis of the PCA (65% variance

171   explained) exhibited a gradient contrasting the stations according to their contamination by TMs

172   (MA5 and CF20 vs. CF29 and CF28). The density and the biomass of earthworms were

173   negatively correlated to the concentrations of TMs in soils. The second and third axis of the

174   PCA (16% and 13% variance explained, respectively) separated stations according to the soil

175   texture (axis 2) and pH/OM content (axis 3). Among soil characteristics, the texture is

176   correlated, negatively for sand content and positively for clay content, to the density and

177   biomass of earthworms.

178   **3-2- Bioaccumulation of TMs by earthworms**

179   The regressions between TM concentrations in whole earthworm tissues and their levels

180   in soils showed significant dose-response relationships for Ag, As, Co, and Pb, but not for Cd

181   ($p = 0.755$) (Fig. 3A and Table S1). The consideration of the earthworm ecological group did

182   not improve the regression for Cd but allowed to distinguish different responses for the other

183   TMs considered (Fig. 3B). Hence, for Co, only endogeic earthworms showed internal

184   concentrations significantly increasing with soil contamination ($p = 0.014$, Table S1). For Ag,

185   a significant and similar relationship between bioaccumulation and soil concentration was

186   highlighted for the epigeics, the endogeics and the epianecics (Fig. 3B and Table S1), while no

187   significance was found for the anecic strict, with average internal concentrations of 0.91 ± 0.26

188   $\mu g\ g^{-1}$. The bioaccumulation of As and Pb by earthworms was important (reaching $103.88\ \mu g_{As}$

189   g^{-1} and $10{,}368.06\ \mu g_{Pb}\ g^{-1}$ on CF28) and was significantly related to soil concentration for all

190   ecological groups (Fig. 3B). More precisely, for these two TMs, the epianecics showed the most

191   marked responses, followed by the endogeics, the epigeics, and finally the anecic strict (Table

192   S1).

193   **3-3- Earthworm density response to TM bioaccumulation**

194   Taking into account all the data, significant and negative relationships were found

195   between earthworm density and their internal concentrations of Ag, As, and Pb. It was not the

196   case for Cd ($p = 0.533$) and Co ($p = 0.133$) (Fig. 4 and Table 4). However, considering each

197   ecological group, various response patterns are highlighted. Thus, it appears that the density of

198   epianecics was negatively affected by the soil contamination for the five TMs considered (Table

199   4). Except for Cd ($p = 0.880$), similar results were reported for endogeic earthworms.

200   Conversely, no significant influence of TM accumulation on the density was observed for the

201   epigeic earthworms for all TMs. Finally, only internal concentrations of As and Pb were

202   significantly associated with a decline in the anecic strict density (Table 4).

203

204   **4- Discussion**

205   **4-1- Bioavailability of legacy contamination**

206   The studied sites were characterized by the presence of various mining wastes deposited

207   several centuries ago, which constitute a chronic and diffuse source of TM release to the

208   surrounding soils (Mariet et al., 2014). Physico-chemical analyses also revealed that the type

209   of mining waste drives the contamination levels in soils and the availability of TMs (Ettler,

210   2016; Mariet et al., 2017b). Hence, the sampled earthworms at the four stations showed marked

211   differences in their internal concentrations of numerous TMs, which testifies to their current

212   bioavailability to earthworms as previously demonstrated for other soil-dwelling invertebrates,

213   i.e., snails (Mariet et al., 2016). Interestingly, earthworms (this study) and snails (Mariet et al.,

214   2016) led to similar observations although these two bioindicators were used in different

215   approaches, i.e., passive and active biomonitoring, respectively. The concentrations of TMs in

216   the earthworm tissues of the control station (MA5) were of the same order as those reported

217   from the literature for non-contaminated forest sites (Ma, 2004; Morgan and Morgan, 1990;

218   Spurgeon and Hopkin, 1996). Lead, Ag, As, and Co bioaccumulation in earthworms respond to

219   their concentrations in the soils while Cd does not. This could be explained by the relatively

220   low concentration of this element in soils and its high leachability, especially under acidic

221   conditions (Rékási and Filep, 2015). The largest TM tissue concentrations were observed for

222   Pb (>10,000 mg kg^{-1} dry weight at CF28) and were comparable to those measured in heavily

223   contaminated sites (Ernst et al., 2008; Ma, 2004). A study recently showed that despite the age

224   of the mining deposits, ageing attenuation was low for Pb, which was still under bioavailable

225   forms (Mariet et al., 2017b). Arsenic reached more than 100 mg kg^{-1} dry weight in earthworms

226   collected at ore dump station CF28, but these values are lower than those found in the literature,

227   even for mining sites (see for instance, Button et al., 2012), probably in relation to the influence

228   of acidic soil pH on As speciation, mobility, and transfer (Wilson et al., 2010). For Ag and Co,

229   the lack of published data concerning their accumulation in earthworms makes the comparisons

230   with our results difficult. However, the significant concentrations measured in earthworms

231   dwelling in mine waste deposit stations (in average 1.3 mg_{Ag} kg^{-1} in CF28 and 5.3 mg_{Co} kg^{-1} in

232   CF29) compared to the control station (MA5) indicate a relatively high exposure to these

233   elements exploited in the valley until the 18th century (Fluck, 2000).

234   Bioaccumulation abilities also depend on the earthworm ecological category. Indeed, in

235   our study, endogeic, and epianecic earthworms showed the highest internal concentrations

236   followed by epigeics and anecic strict. This could be explained by several eco-physiological

237   factors. First, species differences in tissue metal concentration may largely reflect differences

238   in niche separation (Morgan and Morgan, 1999; Qiu et al., 2014). The vertical distribution of

239   different species in the soil profile determines to some extent the exposure of earthworms to

240   contrasted TM bioavailable pools. For instance, epigeic earthworms are less exposed than

241   geophagous species due to their saprophagous feeding behavior on the surface organic horizons

242   of soils and their limited exposure route through dermal surface (Langdon et al., 2003). The

243   results concerning earthworms belonging to the anecic strict category confirm the general

244   tendency toward lower metal contents in tissues of deep-burrowing species (Ernst et al., 2008;

245   Suthar et al., 2008; Tischer, 2009). However, this result was not really expected in our particular

246   context of ancient mining contamination characterized by an increasing contamination with

247   depth. The anecic strict are therefore exposed to elevated total TM concentrations but only low

248   available fractions due to the sequestration of TMs, and especially Pb, in the mineral matrix of

249   ore fragments in soils (Mariet et al., 2017b). The endogeics were the only ecological category

250   to bioaccumulate all five TMs studied significantly. In comparison to the anecic species, which

251   create permanent vertical galleries, the horizontal burrowing system of endogeics may retain

252   more pore water and consequently increase the bioavailability of TMs and transfer through

253   cutaneous uptake (Suthar et al., 2008; Vijver et al., 2003). Lastly, various physiological abilities

254   may also explain the contrasted bioaccumulations observed between earthworms belonging to

255   different ecological categories. Thus, digestive physiology may modulate the assimilation

256 efficiencies of different species (Peijnenburg et al., 2012; Piearce, 1978). Moreover, once

257 assimilated, species-specific biochemical strategies may determine the internal fate of TMs and

258 their subcellular fractionation (detoxification and storage, interaction with sites of toxic action,

259 excretion) (Leveque et al., 2013; Morgan and Morgan, 1992; Morgan and Morgan, 1998; Vijver

260 et al., 2006). The physiological processes involved in the contrasted bioaccumulation patterns

261 need further studies since they may explain the responses of earthworms we observed at the

262 community level.

263

264 **4-2- Community responses to contamination**

265 On the uncontaminated station (MA5), total earthworm density reaches 57 ± 19 ind m^{-2},

266 which is in the range of data reported for European forests (De Wandeler et al., 2016). The

267 distribution within ecological categories is however different with about 7% epigeic, 34%

268 epianecic, 40% anecic strict, and 19% endogeic, reflecting site-specific conditions of the studied

269 area. As an example, we found *Allolobophora zicsii*, an endemic endogeic earthworm species

270 of the Vosges Mountains. A significant decrease of total earthworm density was observed at

271 the stations impacted by mining waste deposits. At the ecological group level, this decline

272 mainly relies on a strong decrease of endogeic and a near-disappearance of anecic and

273 especially anecic strict, which were not retrieved in the CF28 station. More precisely, the results

274 clearly indicate a relationship between the concentrations of TMs accumulated in earthworm

275 tissues and the decline in the density of endogeic and (epi)anecic. Among the TMs studied, Ag,

276 As, and Pb seem particularly involved with internal concentrations exceeding the toxicity

277 thresholds. Indeed, Luo et al. (2014) estimated Pb LC50 (the concentration causing 50 %

278 mortality), EC10, and EC50 (the concentrations causing 10% and 50% effect) values on the

279 survival and reproduction of the earthworm *Eisenia andrei* at 852, 248, and 484 mg$_{Pb}$ kg^{-1}

280 earthworm tissue, respectively. For As, Bustos et al. (2015) determine EC10, 25 and 50 for

281　*Eisenia fetida* response of cocoon production at 38, 47 and 57 mg_{As} kg^{-1}, respectively. Thus,

282　with internal concentrations reaching more than 10,000 and 100 mg kg^{-1} for Pb and As,

283　respectively, these TMs may have cause fitness disturbances (growth, reproduction) at the

284　individual scale and therefore disruptions of the population structure. Toxicity data for Ag and

285　Co for earthworms are, to our knowledge, not available in the literature.

286　　　　Nevertheless, small populations of earthworms, with particular ecological distribution,

287　are still able to survive even under such heavy exposure to TMs, suggesting potential local

288　adaptation of natural populations. Although no definitive evidence has been clearly

289　demonstrated for earthworms, several recent results suggest that TMs may act as selective

290　pressures in natural populations and that genetic variation exists for genes involved in

291　homeostatic regulation and detoxification of TMs (Anderson et al., 2013; Pauwels et al., 2013;

292　Spurgeon et al., 2011).

293　　　　Finally, beyond the soil contamination, it is well established that other edaphic factors

294　also influence the incidence of earthworms in the environment (De Wandeler et al., 2016). In

295　the present study, the mining operations carried out on the different sites have also disturbed

296　the soil structure and texture. On CF20, the digging of mining wells led to the accumulation of

297　relatively small amounts of excavated materials in comparison to CF28, an ore dump dating

298　back to the 17th century, where tons of tailings (coarse gravel and sand) have been deposited

299　during the mine exploitation. CF29 has been a site of ore washing operations and is

300　characterized by the accumulation of fine and dense particles forming compacted layers (former

301　decantation basins). These specific soil features may likely complicate the activity of

302　earthworms, especially for deep-burrowing species such as anecic strict which have almost

303　completely disappeared at stations CF28 and CF29.

304

305　　　**5- Conclusion**

306   Although literature is full of ecotoxicological studies regarding the effects of recent

307 industrial contamination on earthworms, there is a lack of data regarding legacy impact related

308 to very ancient mining activities. Here, we demonstrated using a passive biomonitoring

309 campaign that even several centuries after their deposits, TMs from mining wastes are still

310 bioavailable for local earthworm populations. The related TM accumulation in earthworm

311 tissues, along with the disturbance of soil structure, may explain the decline observed in

312 earthworm density and the disturbance of the ecological distribution marked by the decrease of

313 endogeic and anecic species. It also represents significant loads of TMs potentially transferable

314 to the higher trophic levels. From a management point of view, this study finally points out the

315 necessity to consider ancient mining or smelting wastes as still currently hazardous materials

316 which should be included in the framework of ecological risk assessment of polluted soils and

317 sites.

318

326

327 **Supplementary Data**: Figure S1 represents the biomass of earthworms for each ecological

328 group for the four stations. Table S1 gives the model outputs of the relationships between trace

329 metal concentrations in earthworm tissue (mg kg^{-1}) and concentrations in soil.

330

References

Anderson, C.J., Kille, P., Lawlor, A.J., Spurgeon, D.J., 2013. Life-history effects of arsenic toxicity in clades of the earthworm *Lumbricus rubellus*. Environmental Pollution 172, 200–207.

Bouché, M.B., 1972. Lombriciens de France. Ecologie et Systématique. I.N.R.A. (Annales de Zoologie Ecologie Animale N∘ H.S. 72/2), Paris.

Bouché, M.B., 1977. Stratégies Lombriciennes. Bulletin Ecologie Paris 25, 122–132.

Bustos, V., Mondaca, P., Verdejo, J., Sauvé, S., Gaete, H., Celis-Diez, J.L., Neaman, A., 2015. Thresholds of arsenic toxicity to *Eisenia fetida* in field-collected agricultural soils exposed to copper mining activities in Chile. Ecotoxicology and Environmental Safety 122, 448–454.

Button, M., Koch, I., Reimer, K.J., 2012. Arsenic resistance and cycling in earthworms residing at a former gold mine in Canada. Environmental Pollution 169, 74–80.

De Wandeler, H., Sousa-Silva, R., Ampoorter, E., Bruelheide, H., Carnol, M., Dawud, S.M., Danila, G., Finer, L., Hättenschwiler, S., Hermy, M., Jaroszewicz, B., Joly, F.-J., Müller, S., Pollastrini, M., Ratcliffe, S., Raulund-Rasmussen, K., Selvi, F., Valladares, F., Van Meerbeek, K., Verheyen, K., Vesterdal, L., Muys, B., 2016. Drivers of earthworm incidence and abundance across European forests. Soil Biology & Biochemistry 99, 167–178.

Ernst, G., Zimmermann, S., Christie, P., Frey, B., 2008. Mercury, cadmium and lead concentrations in different ecophysiological groups of earthworms in forest soils. Environmental Pollution 156, 1304–1313.

Ettler, V., 2016. Soil contamination near non-ferrous metal smelters: A review. Applied Geochemistry 64, 56–74.

355   Fluck, P., 2000. Sainte-Marie-aux-Mines ou Les mines du rêve. Une monographie des mines

356   d'argent. Soultz: Les Editions du Patrimoine Minier.

357   Fluck, P., 2006. Les mines de plomb, cuivre et argent de la Renaissance ont généré des paysages

358   contrastés. L'exemple de l'Alsace et des Vosges (France de l'Est).

359   Langdon, C.J., Piearce, T.G., Meharg, A.A., Semple, K.T., 2003. Interactions between

360   earthworms and arsenic in the soil environment: a review. Environmental Pollution 124,

361   361–373.

362   Leveque, T., Capowiez, Y., Schreck, E., Mazzia, C., Auffan, M., Foucault, Y., Austruy, A.,

363   Dumat, C., 2013. Assessing ecotoxicity and uptake of metals and metalloids in relation

364   to two different earthworm species (*Eiseina hortensis* and *Lumbricus terrestris*).

365   Environmental Pollution 179, 232–241.

366   Luo, W., Verweij, R.A., van Gestel, C.A.M., 2014. Determining the bioavailability and toxicity

367   of lead contamination to earthworms requires using a combination of physicochemical

368   and biological methods. Environmental Pollution 185, 1–9.

369   Ma, W.-C., 2004. Estimating heavy metal accumulation in oligochaete earthworms: a meta-

370   analysis of field data. Bulletin of Environmental Contamination and Toxicology 72,

371   663–670.

372   Mariet, A.-L., de Vaufleury, A., Bégeot, C., Walter-Simonnet, A.-V., Gimbert, F., 2016.

373   Palaeo-pollution from mining activities in the Vosges Mountains: 1000 years and still

374   bioavailable. Environmental Pollution 214, 575–584.

375   Mariet, A.-L., Gimbert, F., Bégeot, C., Gauthier, J., Fluck, P., Walter-Simonnet, A.V., 2014.

376   Palaeoenvironmental and actual research on contamination by trace metals on the

377   mining district of Sainte-Marie-aux-Mines, Vosges Mountains. In: Collection Edytem

378   Exploitations minières passées et présentes : impacts environnementaux et sociétaux (in

379   French).

380   Mariet, A.-L., Pauget, B., de Vaufleury, A., Bégeot, C., Walter-Simonnet, A.-V., Gimbert, F.,
381   2017a. Using bioindicators to assess the environmental risk of past mining activities in
382   the Vosges Mountains (France). Ecological Indicators 75, 17–26.
383   Mariet, A.-L., Sarret, G., Bégeot, C., Walter-Simonnet, A.-V., Gimbert, F., 2017b. Lead highly
384   available in soils centuries after metallurgical activities. Journal of Environmental
385   Quality. Special Issue: Synchrotron radiation-based methods for environmental
386   biogeochemistry.
387   Morgan, A.J., Morgan, J.E., 1992. The accumulation and intracellular compartmentation of
388   cadmium, lead, zinc and calcium in two earthworm species (*Dendrobaena rubida* and
389   *Lumbricus rubellus*) living in highly contaminated soil. Histochemistry 75, 269–285.
390   Morgan, J.E., Morgan, A.J., 1990. The distribution of cadmium, copper, lead, zinc and calcium
391   in the tissues of the earthworm *Lumbricus rubellus* sampled from one uncontaminated
392   and four polluted soils. Oecologia 84, 559–566.
393   Morgan, J.E., Morgan, A.J., 1998. The distribution and intracellular compartmentation of
394   metals in the endogeic earthworm *Aporrectodea caliginosa* sampled from an unpolluted
395   and a metal-contaminated site. Environmental Pollution 99, 167–175.
396   Morgan, J.E., Morgan, A.J., 1999. The accumulation of metals (Cd, Cu, Pb, Zn and Ca) by two
397   ecologically contrasting earthworm species (*Lumbricus rubellus* and *Aporrectodea*
398   *caliginosa*): implications for ecotoxicological testing. Applied Soil Ecology 13, 9–20.
399   Nahmani, J., Lavelle, P., Lapied, E., van Oort, F., 2003. Effects of heavy metal soil pollution
400   on earthworm communities in the north of France. Pedobiologia 47, 663–669.
401   Pauwels, M., Frérot, H., Souleman, D., Vandenbulcke, F., 2013. Using biomarkers in an
402   evolutionary context: Lessons from the analysis of biological responses of oligochaete
403   annelids to metal exposure. Environmental Pollution 179, 343–350.

404   Peijnenburg, W., Capri, E., Kula, C., Liess, M., Luttik, R., Montforts, M., Nienstedt, K.,

405   Römbke, J., Sousa, J.P., Jensen, J., 2012. Evaluation of Exposure Metrics for Effect

406   Assessment of Soil Invertebrates. Critical Reviews in Environmental Science and

407   Technology 42, 1862–1893.

408   Pelosi, C., Bertrand, M., Capoweiz, Y., Boizard, H., Estrade, J. R., 2009. Earthworm collection

409   from agricultural fields: Comparisons of selected expellants in presence/absence of hand

410   sorting. European Journal of Soil Biology 45, 176–183.

411   Pérès, G., Vandenbulcke, F., Guernion, M., Hedde, M., Beguiristain, T., Douay, F., Houot, S.,

412   Piron, D., Richard, A., Bispo, A., Grand, C., Galsomies, L., Cluzeau, D., 2011.

413   Earthworm indicators as tools for soil monitoring, characterization and risk assessment.

414   An example from the national Bioindicator programme (France). Pedobiologia 54S,

415   S77–S87.

416   Piearce, T.P., 1978. Gut contents of some lumbricid earthworms. Pedobiologia 18, 153–157.

417   Qiu, H., Peijnenburg, W.J.G.M., van Gestel, C.A.M., Vijver, M.G., 2014. Can commonly

418   measurable traits explain differences in metal accumulation and toxicity in earthworm

419   species? Ecotoxicology 23, 21–32.

420   Rékási, M., Filep, T., 2015. Factors determining Cd, Co, Cr, Cu, Ni, Mn, Pb and Zn mobility

421   in uncontaminated arable and forest surface soils in Hungary. Environmental Earth

422   Sciences 74, 6805–6817.

423   R Core Team, 2014. R: A language and environment for statistical computing. R Foundation

424   for Statistical Computing, Vienna, Austria. URL: http://www.R-project.org

425   Singh, J., Singh, S., Vig, A.P., 2016. Extraction of earthworm from soil by different sampling

426   methods: a review. Environment, Development and Sustainability 18, 1521–1539.

427   Spurgeon, D.J., Hopkin, S.P., 1996. The effects of metal contamination on earthworm
428   populations around a smelting works – quantifying species effects. Applied Soil
429   Ecology 4, 147–160.

430   Spurgeon, D.J., Lister, L., Kille, P., Pereira, M.G., Wright, J., Svendsen, C., 2011.
431   Toxicokinetic studies reveal variability in earthworm pollutant handling. Pedobiologia
432   54S, S217–S222.

433   Suthar, S., Singh, S., Dhawan, S., 2008. Earthworms as bioindicator of metals (Zn, Fe, Mn, Cu,
434   Pb and Cd) in soils: Is metal bioaccumulation affected by their ecological category?
435   Ecological Engineering 32, 99–107.

436   Tischer, S., 2009. Earthworms (Lumbricidae) as bioindicators: the relationship between in-soil
437   and in-tissue heavy metal content. Polish Journal of Ecology 57, 513–523.

438   Tondoh, J.E., Monin, L.M., Tiho, S., Csuzdi, C., 2007. Can earthworms be used as bio-
439   indicators of land-use perturbations in semi-deciduous forest? Biology and Fertility of
440   Soils 43, 585–592.

441   Tylecote, R.F., 1987. The early history of metallurgy in Europe. Longman archaeology series.
442   London. 391 p.

443   Vijver, M.G., van Gestel, C.A.M., van Straalen, N.M., Lanno, R.P., Peijnenburg, W.J.G.M.,
444   2006. Biological significance of metals partitioned to subcellular fractions within
445   earthworms (*Aporrectodea caliginosa*). Environmental Toxicology and Chemistry 25,
446   807–814.

447   Vijver, M.G., Vink, J.P.M., Miermans, C.J.H., van Gestel, C.A.M., 2003. Oral sealing using
448   glue: a new method to distinguish between intestinal and dermal uptake of metals in
449   earthworms. Soil Biology & Biochemistry 35, 125–132.

450   Wilson, S.C., Lockwood, P.V., Ashley, P.M., Tighe, M., 2010. The chemistry and behaviour

451   of antimony in the soil environment with comparisons to arsenic: a critical review.

452   Environmental Pollution 158, 1169–1181.

453 **Table captions**

454

455 **Table 1**: Concentrations of Ag, As, Cd, Co and Pb (μg g^{-1}) for the four stations for three depths

456 (0-5 cm; 5-15 cm; 15-30 cm). Significant differences of concentrations in soils between stations

457 and depths for a TM were highlighted by different letters.

458

459 **Table 2**: Main habitat descriptors of the four stations.

460

461 **Table 3**: Main representative earthworm species sampled in the four stations and for the four

462 ecological groups.

463

464 **Table 4**: Model outputs of the relationships between earthworm density (ind m^{-2}) and their

465 internal concentrations (mg kg^{-1}). Data are given for whole species (total) and each ecological

466 group. SE = Standard Error. For each metal and each model parameter, different letters indicate

467 significant differences.

468

469 **Table 1**

Station	Depth (cm)	Ag	As	Cd	Co	Pb
MA5	0-5	0.34 ± 0.06 [a]	39.97 ± 5.83 [a]	0.35 ± 0.04 [ab]	29.14 ± 8.21 [a]	175.69 ± 24.18 [a]
	5-15	0.75 ± 0.04 [b]	57.92 ± 10.53 [b]	0.29 ± 0.05 [ab]	25.93 ± 5.81 [a]	357.88 ± 53.64 [b]
	15-30	0.14 ± 0.04 [c]	36.24 ± 6.24 [a]	0.26 ± 0.07 [ab]	27.66 ± 4.37 [a]	92.37 ± 11.62 [c]
CF20	0-5	1.10 ± 0.15 [d]	254.89 ± 61.25 [c]	0.41 ± 0.08 [b]	17.74 ± 2.86 [b]	341.63 ± 40.78 [b]
	5-15	0.29 ± 0.05 [a]	150.02 ± 20.13 [d]	0.25 ± 0.04 [a]	18.54 ± 3.13 [b]	177.64 ± 34.72 [a]
	15-30	0.66 ± 0.14 [b]	267.89 ± 56.72 [c]	0.49 ± 0.11 [b]	27.05 ± 6.03 [a]	325.52 ± 87.45 [b]
CF29	0-5	4.69 ± 1.12 [d]	257.85 ± 58.16 [c]	1.10 ± 0.38 [c]	22.99 ± 7.49 [a]	2539.25 ± 374.18 [d]
	5-15	60.41 ± 19.15 [e]	3110.54 ± 514.36 [d]	3.88 ± 0.57 [d]	94.05 ± 23.64 [c]	22,347.63 ± 2795.78 [e]
	15-30	132.23 ± 36.72 [f]	3574.07 ± 427.10 [d]	8.21 ± 0.95 [e]	91.43 ± 8.67 [c]	54,048.87 ± 5708.36 [f]
CF28	0-5	14.80 ± 1.40 [g]	888.25 ± 43.67 [e]	1.33 ± 0.10 [c]	18.12 ± 1.61 [ab]	8582.87 ± 385.3 [g]
	5-15	30.50 ± 1.78 [h]	1658.30 ± 109.92 [f]	2.08 ± 0.18 [f]	29.10 ± 3.46 [a]	12,153.67 ± 849.09 [g]
	15-30	65.79 ± 6.12 [e]	2334.15 ± 145.11 [g]	3.54 ± 2.13 [cdf]	48.72 ± 2.13 [d]	24,748.40 ± 3209 [e]

470

471

472 **Table 2**

Station	Altitude (m a.s.l.)	Dominating tree species	pH water	Clay (g kg⁻¹)	Silt (g kg⁻¹)	Sand (g kg⁻¹)	C_{org} (g kg⁻¹)	CEC (cmol⁺ kg⁻¹)
MA5	730	*Abies alba, Acer pseudoplatanus, Fagus sylvatica*	4.6 ± 0.1	266 ± 31	286 ± 29	448 ± 59	75.5 ± 7.6	25.7 ± 0.6
CF29	782	*Abies alba, Acer pseudoplatanus*	5.0 ± 0.1	99 ± 34	305 ± 139	595 ± 172	19.2 ± 1.6	8.6 ± 1.2
CF28	804	*Abies alba, Picea abies*	4.3 ± 0.1	133 ± 13	242 ± 20	625 ± 33	52.3 ± 17.5	15.5 ± 3.4
CF20	856	*Abies alba, Fagus sylvatica*	4.7 ± 0.05	131 ± 8	234 ± 21	635 ± 28	27.4 ± 5.1	11.9 ± 1.6

473

474   **Table 3**

Station	Epigeic	Endogeic	Epianecic	Anecic strict
MA5	*Lumbricus moliboeus*	*Allolobophora zicsii* *Aporrectodea caliginosa*	*Lumbricus rubellus rubellus* *Lumbricus rubellus friendoides*	*Aporrectodea* sp.
CF20	*Allolobophora antipai (vogesiana?)*	*Aporrectodea caliginosa* *Aporrectodea longa*	*Lumbricus rubellus rubellus*	*Aporrectodea (nocturna?)*
CF28	*Lumbricus* sp.	*Aporrectodea caliginosa*	*Lumbricus rubellus rubellus*	-
CF29	*Lumbricus* sp.	*Allolobophora rosea vedovinii* *Aporrectodea caliginosa*	*Lumbricus rubellus rubellus*	*Aporrectodea* sp.

475

Table 4

Metal	Constant	Total value	SE	p-value	Epigeic value	SE	p-value	Epianecic value	SE	p-value	Anecic strict value	SE	p-value	Endogeic value	SE	p-value
Ag	d0	1.251	0.108	<0.001	0.723 [a]	0.211	0.001	1.517 [b]	0.182	<0.001	1.797 [ab]	0.639	0.007	1.183 [ab]	0.156	<0.001
	-k	-1.721	0.542	0.002	-0.029 [a]	1.197	0.981	-3.075 [b]	0.734	<0.001	-1.768 [ab]	1.306	0.182	-1.890 [ab]	0.695	0.009
As	d0	1.518	0.173	<0.001	0.697 [a]	0.194	<0.001	2.125 [b]	0.359	<0.001	1.999 [b]	0.428	<0.001	1.565 [b]	0.326	<0.001
	-k	-0.444	0.105	<0.001	0.022 [a]	0.189	0.906	-0.733 [b]	0.157	<0.001	-0.478 [b]	0.179	0.010	-0.557 [b]	0.195	0.006
Cd	d0	1.031	0.278	<0.001	0.529 [a]	0.306	0.090	3.855 [a]	1.837	0.041	0.212 [a]	0.209	0.316	0.755 [a]	0.432	0.087
	-k	-0.184	0.293	0.533	0.331 [a]	0.603	0.586	-2.041 [b]	0.694	0.005	1.581 [ac]	0.921	0.093	0.076 [abc]	0.506	0.880
Co	d0	1.348	0.373	<0.001	0.637 [ab]	0.340	0.067	11.03 [ab]	7.205	0.132	0.172 [a]	0.143	0.233	1.872 [b]	0.620	0.004
	-k	-0.644	0.421	0.133	0.175 [ac]	0.761	0.819	-4.090 [b]	1.104	<0.001	2.488 [a]	1.078	0.025	-1.213 [c]	0.509	0.022
Pb	d0	2.129	0.359	<0.001	0.805 [a]	0.273	0.005	2.151 [b]	0.352	<0.001	24.75 [ab]	22.78	0.283	2.843 [b]	0.898	0.003
	-k	-0.332	0.057	<0.001	-0.039 [a]	0.115	0.734	-0.403 [b]	0.083	<0.001	-1.152 [c]	0.351	0.002	-0.443 [bc]	0.122	<0.001

478 **Figure captions**

479

480 **Figure 1**: Distribution of individuals in ecological groups, expressed as density (mean ± S.D.,

481 individuals m^{-2}). Significant differences of density between stations for an ecological group

482 were highlighted by different letters.

483

484 **Figure 2**: Principal component analysis between earthworm community descriptors (total

485 density and biomass), soil contamination (total Ag, As, Cd, Co, and Pb concentrations) and soil

486 characteristics as texture (sand and silt contents), pH, and OM content. Left: Axis 1 and 2;

487 Right: Axis 1 and 3. Stations (MA5, CF20, CF28 and CF29) are also projected.

488

489 **Figure 3**: Modelled relationships between trace metal concentrations in earthworm tissues (mg

490 kg^{-1}) and concentrations in soil (mg kg^{-1}). (A): Model fitted to the whole data. (B): Models fitted

491 to each ecological group. Details about model outputs for each ecological group are given in

492 Table S2.

493

494 **Figure 4**: Modelled relationships between earthworm density (ind m^{-2}) and trace metal

495 concentrations in their tissues (mg kg^{-1}). The model was fitted to the whole data. Details about

496 model outputs for each ecological group are given in Table 4.

497

498 **Figure 1**
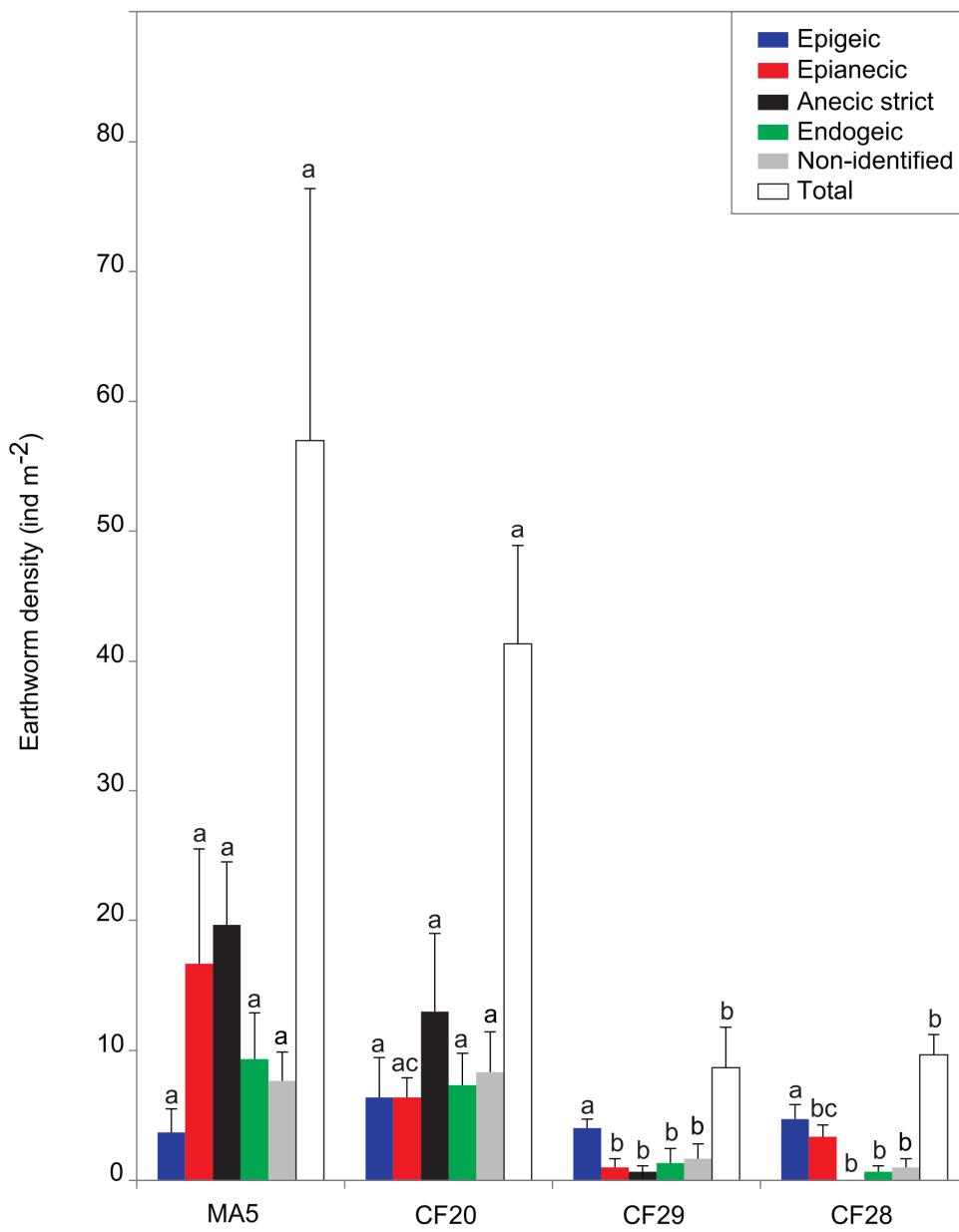
499

500

501 **Figure 2**

502
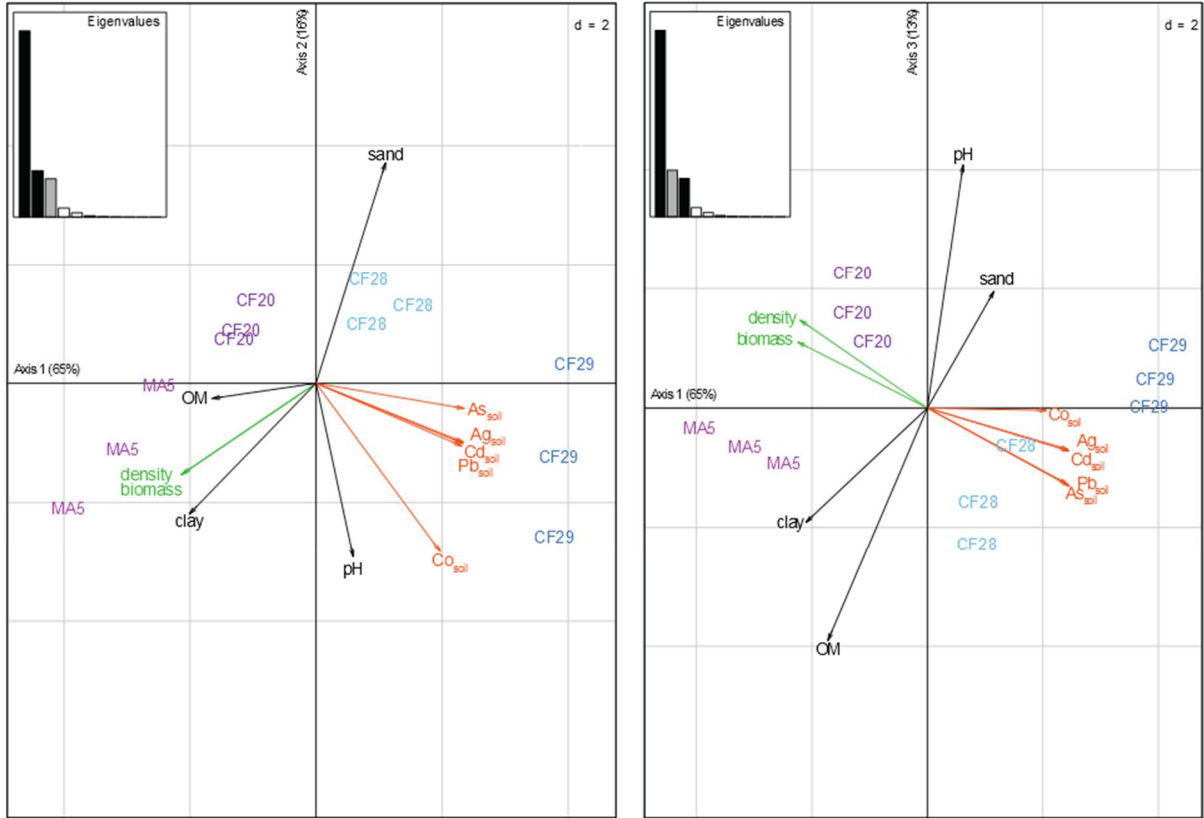
503

504

505   **Figure 3**

506

Figure 4
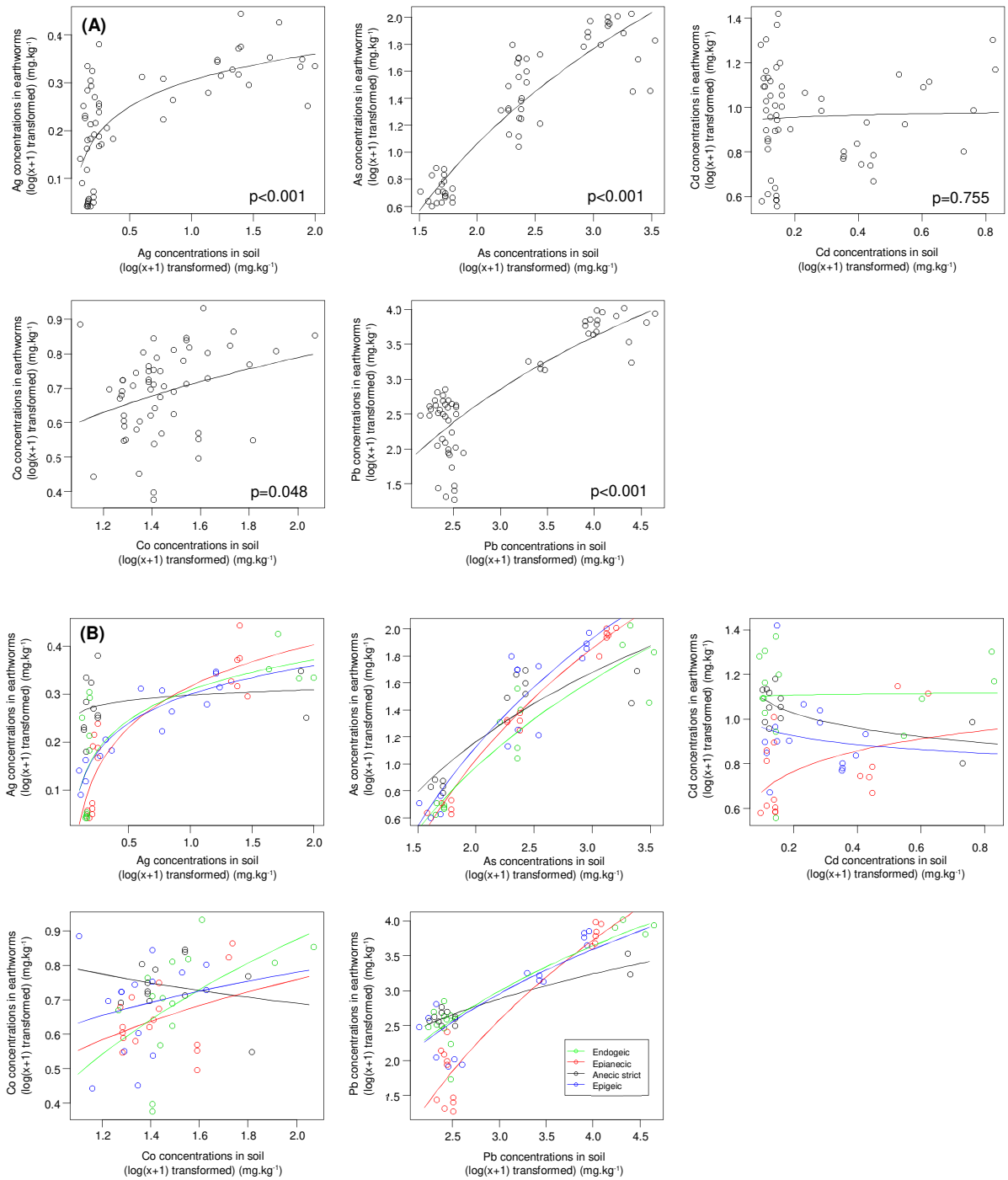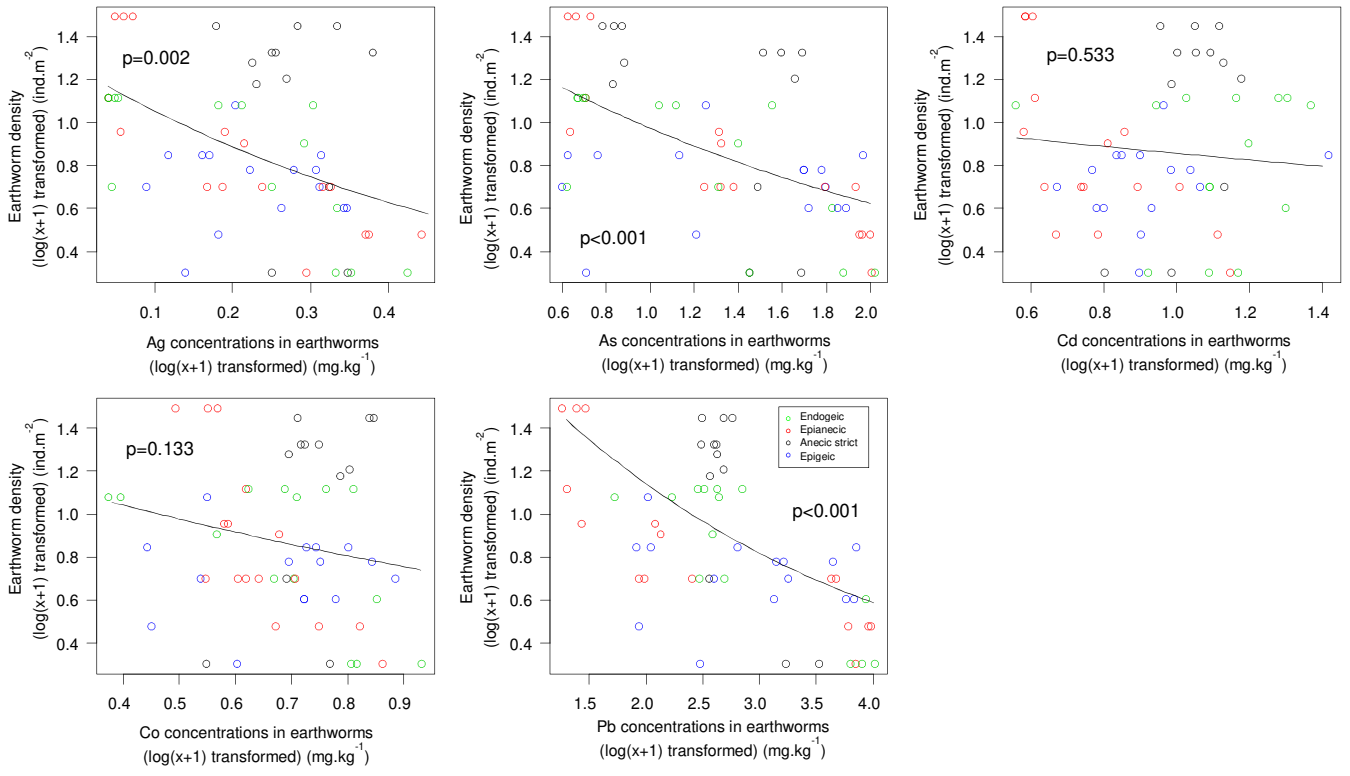
1   **Generated compounds at the V-slag/CaO diffusion surface and diffusion characteristics of V**

2   **and Ca in calcium vanadate**

3   Declarations of interest: none

4   Hong-Rui Yue [1)], Xiang-Xin Xue [1) *]

5   1)   School of Metallurgy, Northeastern University, Shenyang 110819, China

6   Corresponding author: Xiang-Xin Xue; e-mail: xuexx@mail.neu.edu.cn;

7   **Email:** Hong-Rui Yue, hongrui.neu@gmail.com;

8   Xiang-Xin Xue, xuexx@mail.neu.edu.cn;

9
10
11
12
13
14
15
16
17
18
19
20
21
22
23
24
25
26
27
28
29
30
31
32
33
34
35
36
37

Abstract

Vanadium slag/CaO diffusion couples were prepared to study the diffusion characteristics of the vanadium slag/CaO interface at 1083 K in the air. The generated phases at different regions were characterized by EPMA, EDS, XRD, and element maps analysis. At the vanadium slag surface that the diffused Ca dose not reached, the main generated phases were Mn_2O_3 and Fe_2O_3. V^{3+} was oxidized to V^{5+} and reacted with the Ca^{2+} to form a small amount of $Ca_2V_2O_7$. Cr was at a disadvantage compared with V in occupying the original Ca^{2+} of the slag. At the vanadium slag surface that the diffused Ca had reached, the main generated phases were $Ca_2V_2O_7$. At the CaO surface, the main generated phases were $Ca_2V_2O_7$ and $Ca_3V_2O_8$. The interdiffusion coefficients were calculated by a new approach that modified from the Boltzmann-Matano method including the determination of the Matano surface, calculation of the integral and differential using the raw data of the concentration profiles. As the molar fraction of Ca was in the range of 0.15 to 0.86, the average interdiffusion coefficient of Ca^{2+} was 2.54×10^{-8} $cm^2 \cdot s^{-1}$. The average interdiffusion coefficient of V^{5+} at the V molar fraction of 0.001 to 0.43 was 1.96×10^{-8} $cm^2 \cdot s^{-1}$.

keywords: Vanadium slag, calcium roasting, diffusion couple, diffusion coefficient, Boltzmann-Matano method

1. Introduction

Vanadium slag (V-slag) usually refers to the solid slag produced in the converter during smelting the vanadium titanium magnetite. As a byproduct of iron making, V-slag contains a large amount of low-valent V which is often extracted by the process of crushing, iron removal, roasting, leaching, precipitation and calcining, etc. Among these processes, roasting is the first one that

2

61   mainly involves chemical reactions, which makes it more complicated and essential. The primary

62   purpose of roasting is to oxidize the low-valent V in the V spinels into high-valent V and enrich it

63   in the vanadates that can be leached out. At first, sodium salts were proposed as the additives in

64   roasting V-slag, $NaCO_3$ [1,2], mixture of $NaOH$ and $NaNO_3$ [3], or $NaOH$ [4] react with V-slag to

65   generate water-soluble soluble vanadates which can be leached in aqueous solution. Under the

66   optimal conditions, almost 100% V can be recovered from the V-slag [4]. In recent years, the sodium

67   salts were gradually abandoned in the roasting due to the severe groundwater pollution caused by

68   sodium ions [5], and calcium salts were proposed as the roasting additives.

69   Zhang [6] studied the process of roasting V-slag powders with CaO powders by

70   thermogravimetric analysis, and the results showed that the V spinels were oxidized and

71   decomposed as the temperature increasing. When the temperature reached 930 K, the oxidized V

72   begun to react with CaO and form calcium vanadates. Cao [7] and Zhang [8] studied the effect of

73   experimental parameters on the V recovery from roasting V-slag powders with CaO powders. The

74   optimal roasting temperature, roasting time, and mass ratio of CaO to V_2O_5 can be inferred as 1123

75   K, 1.5-2.5 hours, and 0.5-0.7, respectively. The reports about roasting V-slag with CaO are

76   relatively rare, and the research method is limited to simulate the roasting system by mixing the V-

77   slag powders and CaO powders. The species of the generated phases are still controversial, much

78   less the distribution of them around the reaction interface. Therefore, more systematic studies of

79   roasting V-slag with CaO are necessary to carry out, and the research methods that can intuitively

80   reflect the interfacial reaction characteristics should be introduced.

81   Preparing the diffusion couple is an intuitive way to study the properties of the reaction

82   interface by coupling dissimilar materials [9]. Simulating reaction systems can help in understanding

83 the phase transformations and the growth of intermediate phases by diffusion-controlled processes

84 [10]. Usually, two materials of different compositions are joined at a sharp planar interface and

85 subjected to heat treatment at a fixed elevated temperature [11]. In the present work, the V-slag/CaO

86 diffusion couples were prepared and roasted at 1083 K which summarized from the optimal roasting

87 parameters [6-8]. In addition to characterizing the diffusion interface of the V-slag/CaO diffusion

88 couple, a new method was proposed to determine the Matano surface and calculate the interdiffusion

89 coefficients. The concentration profiles obtained by EPMA can be directly applied to the new

90 method.

91
92 **2. Experimental**

93
94 **2.1. Materials**

95
96   Analytical reagent grade CaO was supplied by Sinopharm Chemical Reagent Co., Ltd. V-slag

97 was gathered from HBIS Group ChengSteel Company, and the composition was analyzed by X-ray

98 fluorescence (XRF, ZSX100e, Rigaku, Japan) and listed in Table 1. The CaO powders and V-slag

99 powders were ball-milled by the high energy ball Vario-Planetary Mill (Pulveristte 4, Fritsch,

100 German) for 3 hours. The diameters of CaO powders and V-slag powders were evaluated by field

101 emission scanning electron microscopy (SEM, Ultra Plus, Carl Zeiss GmbH, Jena, Germany) and

102 shown in Fig. 1(a) and Fig. 1(b), respectively. The particle size of CaO and V-slag are distributed

103 around 20 nm and 200 nm, respectively.

104
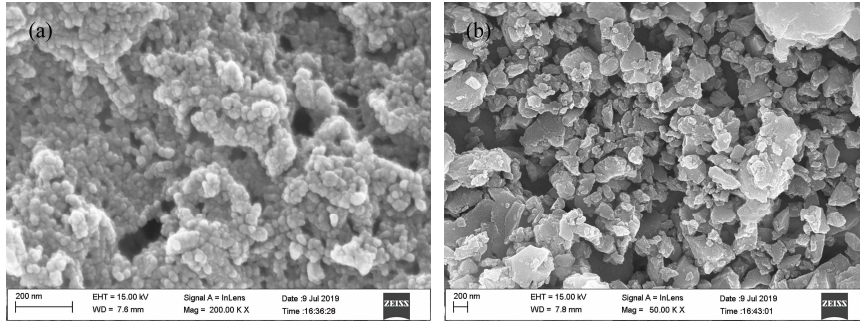
Fig. 1. SEM photographs of CaO particles (a) and raw V-slag particles (b) milled for 3 hours. The ratio of ball to powder was 10:1; the speed of the main-plane and vice-plane were 300 and 150 r/min, respectively; the diameter of the zirconia ball was 10 mm.

Table 1
Chemical composition of the V-slag analyzed by XRF (mass fraction, %)

Fe_2O_3	SiO_2	MnO_2	TiO_2	V_2O_5	MgO	Al_2O_3	CaO	Cr_2O_3
43.4993	14.6256	10.8470	10.2746	8.3874	3.0010	2.6832	2.5803	2.4125

2.2. Preparation of V-slag/CaO diffusion couple

Fig. 2 presents the schematic diagram of preparing the V-slag/CaO diffusion couple. As shown in Fig. 2(a) through Fig. 2(d), the CaO powders were pressed (14130 N) into a pellet of 30 mm diameter and 5 mm thickness in the stainless-steel die. As shown in Fig 2(e) through Fig. 2(h), according to the method [12] that can obtain the dense CaO pellet, here, the CaO pellet was hot-pressed in the graphite die at 1573 K for 120 minutes in the vacuum hot-pressing furnace with the vacuum of 20 Pa. The two circular surfaces of the sintered CaO pellet in Fig. 2(h) were polished using SiC sandpapers (23 µm, 13 µm, and 6.5 µm) with diamond polishing paste (1 µm). As shown in Fig. 2(i) through Fig. 2(l), similar to the embedding method of preparing a diffusion couple [13], here, a quarter of the CaO pellet was embedded into the V-slag powders and pressed (1766 N) into a pellet of 30 mm diameter and 10 mm thickness in a stainless-steel die. As shown in Fig. 2(m)

125   through Fig. 2(p), the V-slag pellet with the CaO pellet were hot-pressed (7065 N) in the graphite

126   die at 1223 K for 90 minutes in the vacuum hot-pressing furnace with the vacuum of 20 Pa. The

127   V-slag/CaO pellet was cut into two pieces, and the diffusion surface was polished using sandpapers

128   and diamond polishing paste. As shown in Fig. 2(q) through Fig. 2(t), the V-slag/CaO diffusion

129   couple was heated to 1083 K and maintained at this temperature for different time in the muffle

130   furnace. The surface directly contacted with the air during the roasting was named $S(xz)$. Besides,

131   the graphite die was coated with boron nitride to prevent carbon contamination.

132
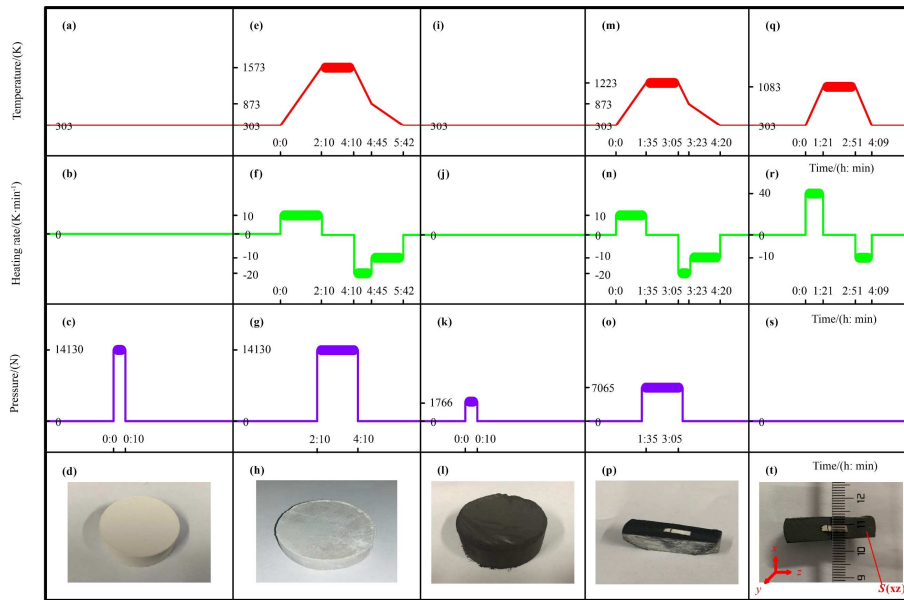
133

134   **Fig. 2**. Schematic diagram of preparing the V-slag/CaO diffusion couple.

135

136   **2.3. Calculation of interdiffusion coefficients**

137

138   Fick's second law was proposed to describe the diffusion flux by the concentration gradient

139   and diffusion coefficient [14]. Matano [15] transformed the partial differential equation of Fick's

140   second law [16] to ordinary differential equation utilizing the Boltzmann parameter [17], and

6

141   suggested using Eq. (1) to determine the variation of the diffusion coefficient with concentration.

142   Eq. (1) which known as the Boltzmann-Matano formula was widely used to calculate the

143   interdiffusion coefficient of the diffusion couple with the initial conditions in Eq. (2) [18]. The

144   integral and differential in Eq. (1) can be graphically expressed by the area (A_{abgf}) and the slope (k)

145   in Fig. 3(a), respectively. Then, the interdiffusion coefficient at a certain concentration (C') can be

146   expressed as Eq. (3). The key to the Boltzmann-Matano method is to find a particular location that

147   satisfies Eq. (4), and this location was named Matano surface [19]. Eq. (4) can be graphically

148   explained as that the area enclosed by C_{a}, C and the Matano surface equals to that enclosed by C_{e},

149   C and the Matano surface. Namely, the critical step is to find the point m on the concentration

150   profiles that makes A_{abm} equals to A_{dem}. However, the concentration profiles of the multiphase

151   materials, such as the V concentration profiles on the V-slag surface in the present work, are always

152   too fluctuant to calculate the integral and differential in Eq. (1). Inspired by the works of Appel [20]

153   and Wagner [21], this paper makes the following modifications to the Boltzmann-Matano method.

154   Firstly, the integral variable in Eq. (4) is changed from dC to dx, and Eq. (4) is expressed as Eq. (5).

155   At the same time, the Riemann integral suggests that the area of a definite integral can be represented

156   by the sum of the areas of the little rectangles. Thus, as shown in Fig. 3(b), the areas defined by C_{a},

157   C and the Matano surface (A_{afh}) and C_{e}, C and the Matano surface (A_{efj}) can be expressed as Eq. (6)

158   and Eq. (7), respectively. As shown in Fig. 3(c), when A_{afh} equals to A_{efj}, the Matano surface (point

159   m) is determined. Secondly, the Matano surface is set as the origin (X=0) of a new X-axis. As shown

160   in Fig. 3(d). A_{abgf} can be expressed as the sum of A_{afh} and A_{hbgf} and calculated as Eq. (8). Thirdly,

161   the slopes are determined numerically using the five-point differentiation formulae [22] as given in

162   Eq. (9) and Eq. (10). Finally, the interdiffusion coefficient can be calculated by Eq. (11). The more

7

163 information about the new method of calculating the interdiffusion coefficient can be seen in our

164 patent [23].

165

166
$$D = -\frac{1}{2t}\frac{\int_{C_a}^{C'} x\,dC}{\left(\frac{dC}{dx}\right)_{C=C'}} \tag{1}$$

167
$$C(x,0) = \begin{cases} C_a, & x < 0 \\ C_e, & x > 0 \end{cases} \tag{2}$$

168
$$D = -\frac{1}{2t}\frac{A_{\text{abgf}}}{k} \tag{3}$$

169
$$\int_{C_a}^{C_m} x\,dC = -\int_{C_m}^{C_e} x\,dC \tag{4}$$

170
$$\int_{x_a}^{x_m} C\,dx = -\int_{x_m}^{x_e} C\,dx \tag{5}$$

171
$$A_{\text{afh}} = \sum_{i=a}^{i=f}(C_a - C_i)\,\Delta x \tag{6}$$

172
$$A_{\text{efj}} = \sum_{i=f}^{i=e}(C_i - C_e)\,\Delta x \tag{7}$$

173
$$A_{\text{abgf}} = \begin{cases} \sum_{i=a}^{i=f}(C_a - C_i)\,\Delta X + (C_a - C')(0 - X_{c'}), & X < 0 \\ \sum_{i=f}^{i=e}(C_i - C_e)\,\Delta X + (C' - C_e)(X_{c'} - 0), & X > 0 \end{cases} \tag{8}$$

174 For interior points:

175
$$k = \frac{1}{12\Delta X}(C_{X'-2\Delta X} - 8C_{X'-\Delta X} + 8C_{X'+\Delta X} - C_{X'+2\Delta X}) \tag{9}$$

176 For end-points:

177
$$k = \frac{1}{12\Delta X}(-25C_{X'} + 48C_{X'+\Delta X} - 36C_{X'+2\Delta X} + 16C_{X'+3\Delta X} - 3C_{X'+4\Delta X}) \tag{10}$$

178
$$D = \begin{cases} -\dfrac{1}{2t}\dfrac{\sum_{i=a}^{i=f}(C_a - C_i)\Delta X + (C_a - C')\left(0 - X_{c'}\right)}{\frac{1}{12\Delta X}(C_{X'-2\Delta X} - 8C_{X'-\Delta X} + 8C_{X'+\Delta X} - C_{X'+2\Delta X})}, & X < 0,\ \text{interior points} \\[2.5em] -\dfrac{1}{2t}\dfrac{\sum_{i=f}^{i=e}(C_i - C_e)\Delta X + (C' - C_e)(X_{c'} - 0)}{\frac{1}{12\Delta X}(C_{X'-2\Delta X} - 8C_{X'-\Delta X} + 8C_{X'+\Delta X} - C_{X'+2\Delta X})}, & X > 0,\ \text{interior points} \\[2.5em] -\dfrac{1}{2t}\dfrac{\sum_{i=a}^{i=f}(C_a - C_i)\Delta X + (C_a - C')(0 - X_{c'})}{\frac{1}{12\Delta X}(-25C_{X'} + 48C_{X'+\Delta X} - 36C_{X'+2\Delta X} + 16C_{X'+3\Delta X} - 3C_{X'+4\Delta X})}, & X < 0,\ \text{end-points} \\[2.5em] -\dfrac{1}{2t}\dfrac{\sum_{i=f}^{i=e}(C_i - C_e)\Delta X + (C' - C_e)(X_{c'} - 0)}{\frac{1}{12\Delta X}(-25C_{X'} + 48C_{X'+\Delta X} - 36C_{X'+2\Delta X} + 16C_{X'+3\Delta X} - 3C_{X'+4\Delta X})}, & X > 0,\ \text{end-points} \end{cases} \tag{11}$$

179

180 Where D is the interdiffusion coefficient (cm$^2\cdot$s^{-1}). C is the concentration (g or mol). t is the time

181 (s). x is the location on the x-axis (μm). A is the area (μm^2). k is the slope. X is the location on the

8

182   *X*-axis (µm).

183
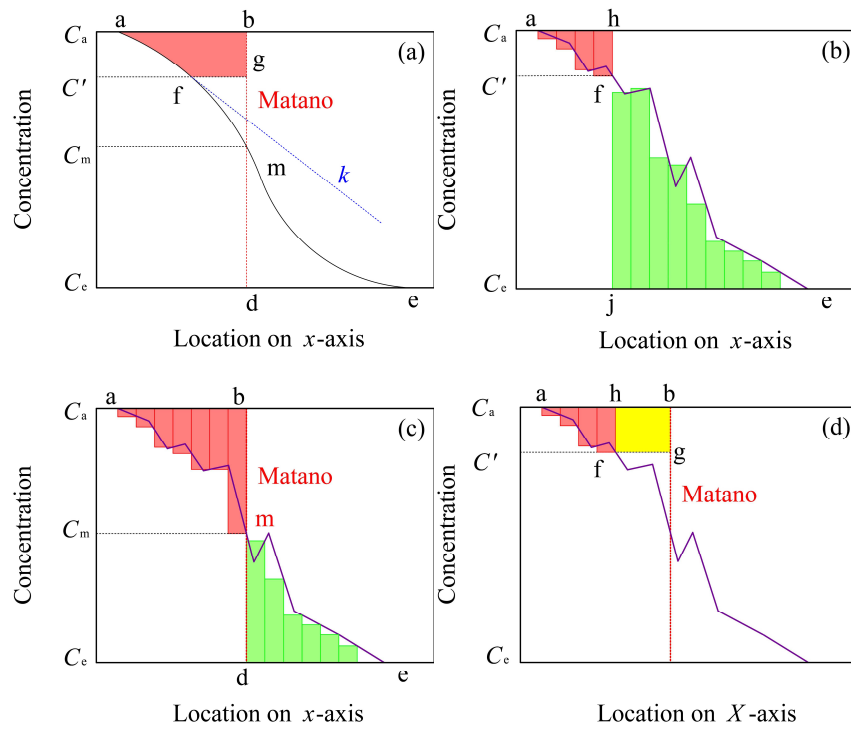
186   **Fig. 3.** Graphical interpretation of calculating the interdiffusion coefficient based on the Boltzmann-

187   Matano method.

188

189   **2.4. Characterization**

190

191   The diffusion surface sprayed of C was analyzed by the electron probe microanalysis (EPMA,

192   JXA-8530F, JEOL, Japan) with the accelerating voltage of 15 kV. The crystalline phases at different

193   locations on the diffusion surface were identified by the X-Ray diffraction (XRD, SmartLab, Rigaku,

194   Japan) with Cu Kα radiation (λ=1.54056Å), scanning area of 0.5 mm × 0.5 mm, and scanning rate

195   of 5º/min.

196

197   **3.   Results**

9

198

3.1. The thickness of the transport layer at $S(xz)$ before roasting in the air

200

201   The cross-sectional views of the diffusion interface before roasting in the air are shown in Fig.

202   4(a) and 4(b). The red dashed curve and the yellow dashed curve represent the ending diffusion

203   boundary of Ca on the V-slag surface and the ending diffusion boundary of V on the CaO surface,

204   respectively. A narrow transport layer (L_0), 25.5 µm approximately, is presented at the diffusion

205   surface, which means the degree of the reaction between the low-valent V and CaO is very slight.

206   Detecting of concentration by EPMA is performed along the scale line 4-1 in Fig. 4(a) and Fig. 4(b),

207   and the raw data are plotted in Fig. 4(c). From 15 µm to 40 µm, the V profiles show a general

208   downward trend; the Ca profiles present a general upward trend. While, the fluctuating data can also

209   be seen both on the V profiles and Ca profiles, especially that on the V-slag surface. As given in

210   Table 1, the V-slag already contains a small amount of Ca before roasting, and the generated phases

211   after roasting are very complicated. Therefore, it is challenging to precisely determine the ending

212   diffusion boundary of Ca on the V-slag surface by the following SEI-SEM photographs, COMPO-

213   SEM photographs or the concentration profiles.

214

215
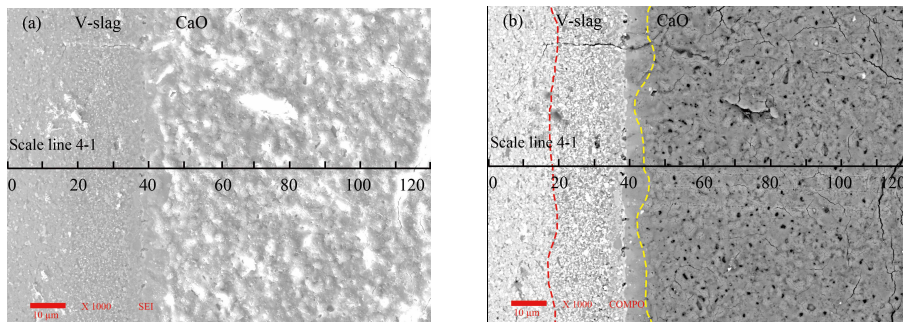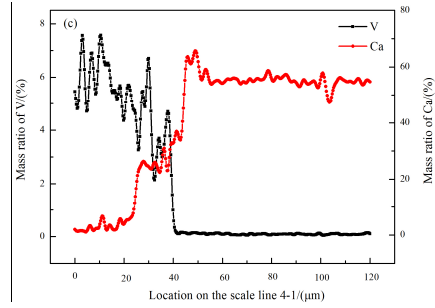
Fig. 4. Cross-sectional views and concentration profiles of the V-slag/CaO interface annealed at

1223 K for 1.5 hours with the vacuum of 20 Pa.

3.2. The diffusion of V and Ca at S(xz) roasted in the air with different time

The cross-sectional views of the diffusion interface after roasting in the air for different time

and the corresponding concentration profiles are shown in Fig. 5. As illustrated in Fig. 5, the

diffusion thickness (L_x) increases with the increase of the roasting time. The diffusion thickness is

evaluated by the graphical method [24], and it shows a linear relationship with the square root of

roasting time as illustrated in Fig. 6. As usual, three theories were proposed to explain the migration

during the diffusion process: the interstitial mechanism [25], the substitutional mechanism [26], and

the vacancy mechanism that was widely accepted in metallurgy [27-29]. The vacancy mechanism

is that a rise in temperature increases the diffusive mobility of cations; some of them overcome the

potential barrier (binding energy in the crystal lattice) and jump [30,31]. The jumped cations diffuse

in counter directions toward each other through the cation vacancies and maintain the electrical

neutrality at the diffusion interface. The reactions between V_2O_5 and CaO in roasting V-slag were

reported [6] as Eqs. (12)-(14). At the same time, the diffusion rate of Ca^{2+} is faster than that of V^{5+}

in the calcium vanadates as calculating in the following section. Thus, the reaction mechanism may

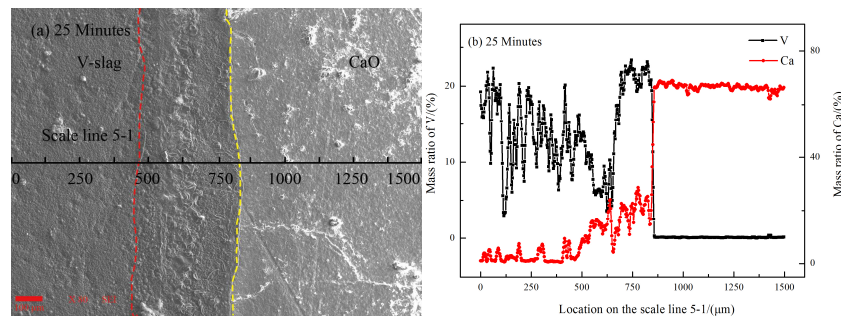be that once the V-slag/CaO diffusion couple is heated to the reaction temperature, calcium

11

235 vanadates begin to form at the V_2O_5/CaO interface. Ca^{2+} diffuses toward V_2O_5 through Ca^{2+}

236 vacancies, and holes (*h*) diffuse in the counter direction to maintain the electrical neutrality in the

237 calcium vanadates. The diffused Ca^{2+} reacts with V_2O_5 to form calcium vanadates and generate

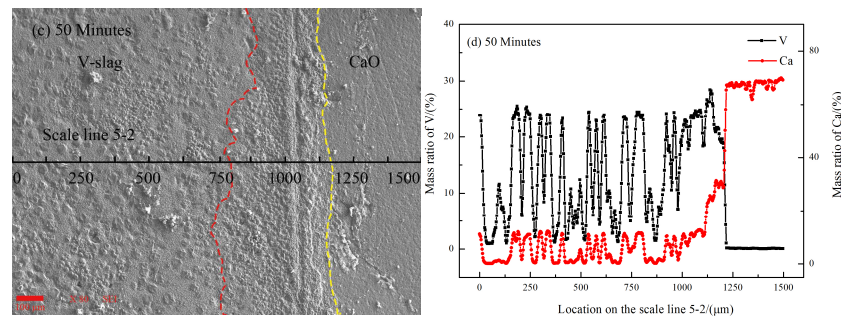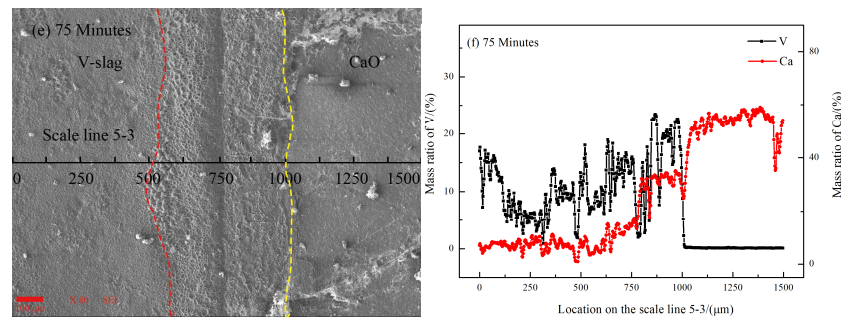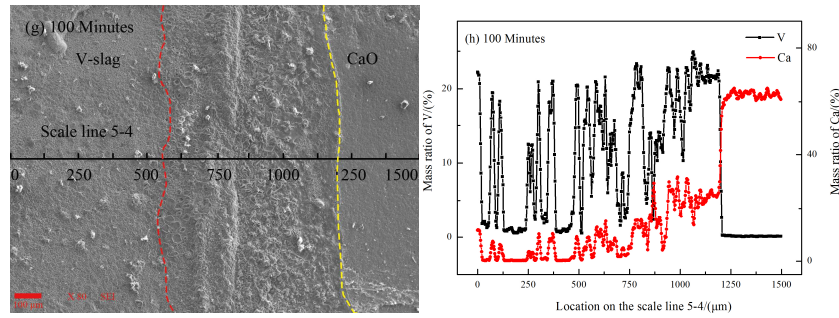238 holes at the calcium vanadates/V_2O_5 interface as given in Eqs. (15)-(17).

239

$$V_2O_5 + CaO = CaV_2O_6 \tag{12}$$

240

$$V_2O_5 + 2CaO = Ca_2V_2O_7 \tag{13}$$

241

$$V_2O_5 + 3CaO = Ca_3V_2O_8 \tag{14}$$

242

243
$$Ca^{2+} + V_2O_5 + \frac{1}{2}O_2(g) = CaV_2O_6 + 2h \tag{15}$$

244
$$2Ca^{2+} + V_2O_5 + O_2(g) = Ca_2V_2O_7 + 4h \tag{16}$$

245
$$3Ca^{2+} + V_2O_5 + \frac{3}{2}O_2(g) = Ca_3V_2O_8 + 6h \tag{17}$$

246

247

248

249

12

250
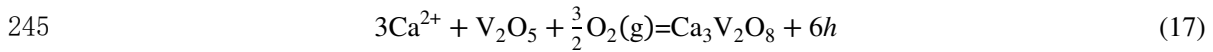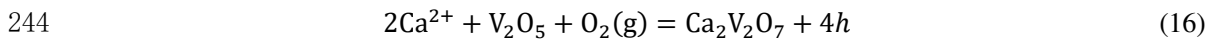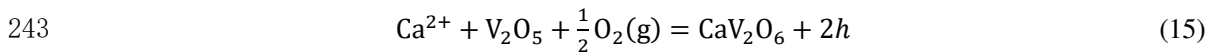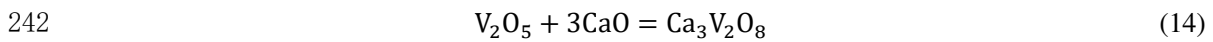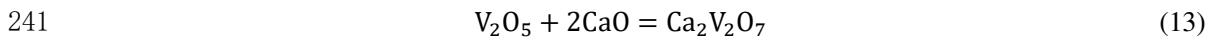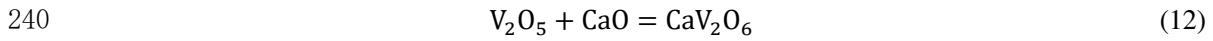
Fig. 5. Cross-sectional views and concentration profiles of the V-slag/CaO interface after annealing

at 1083 K in the air for different time.

254
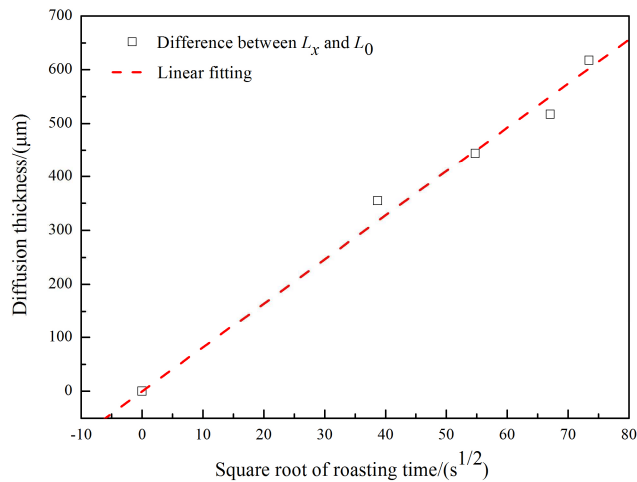
Fig. 6. Relationship between the roasting time and the diffusion thickness at the diffusion surface

annealing at 1083 K in the air. The linear fitting coefficient of R^2 is 0.9965.

3.3. Evolution of the main generated compounds with the location at $S(xz)$

Fig. 7 is the phase diagram of the V_2O_5-CaO system from 273 K to 3273 K calculated by the

FactSage. As thermodynamic predicting in Fig. 7, three new phases of CaV_2O_6, $Ca_2V_2O_7$ and

$Ca_3V_2O_8$ could be formed during annealing at 1083 K. The microscopic characteristics of the $S(xz)$

roasted for 75 minutes in the air are shown in Fig. 8(a). The enlarged drawings and EDS analysis of
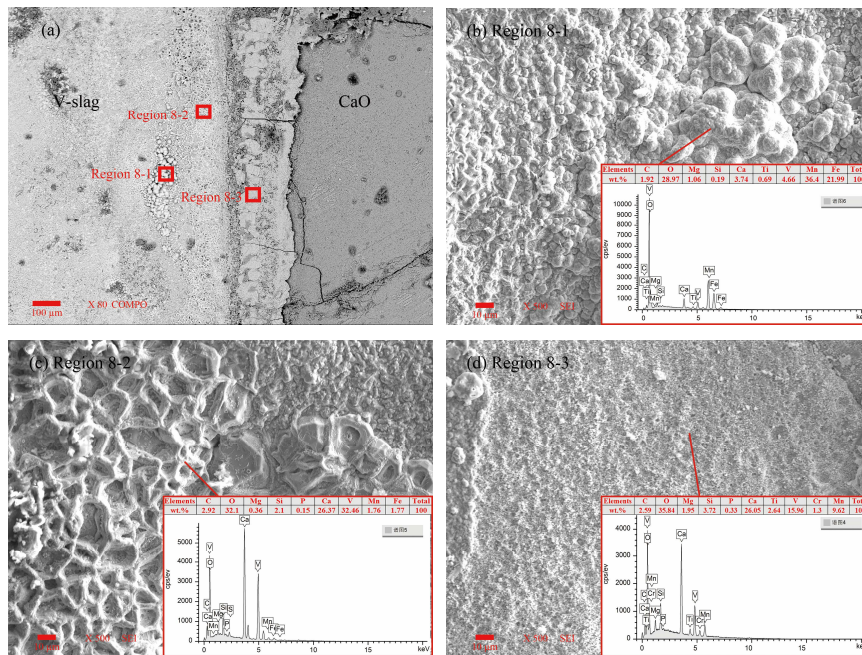
the generated compounds at different locations in Fig. 8(a) are shown in Fig. 8(b), Fig. 8(c), and

265 Fig. 8(d). As illustrated in Fig. 8(b), the spherical compounds are mainly composed of Mn, Fe, and

266 O with the total mass fraction accounting for 89.07 (regardless of the spraying C). According to the

267 reported XRD analysis [32,33], $(Mn,Fe)(V,Cr)_2O_4$ decomposed during the blank roasting of V-slag,

268 Fe was mainly gathered in Fe_2O_3, Mn was enriched in $Mn_2V_2O_7$. In this case, region 8-1, where the

269 diffused Ca doesn't reach, can also be considered as a blank roasting area. However, the conclusion

270 of quantitative analysis (EDS) in Fig. 8(b) is not the same as the conclusion of qualitative analysis

271 (XRD) in the literature [32], namely, only a small amount of divalent Mn may be gathered into

272 $Mn_2V_2O_7$. Besides, another literature [6] reported that V_2O_5 was preferentially formed calcium

273 vanadates with Ca rather than manganese vanadates with Mn. Only the content of Ca was

274 insufficient could the excess V_2O_5 form manganese vanadates with the divalent Mn which was not

275 oxidized in advance by oxygen. Thus, it can be extracted from the literature [6] and the result in Fig.

276 8(b) that most of Mn should be preferentially enriched in manganese oxides. As shown in Fig. 8(c),

277 the generated compounds on the V-slag surface and near the V-slag/CaO interface have the bowl-

278 shaped appearance, and the main components are Ca, V, and O that account for 93.67 mass fraction

279 in total. If the oxygen occupied by SiO_2, MgO, P_2O_5, MnO_2, and Fe_2O_3 are excluded, the chemical

280 formula of the generated compounds can be calculated as $Ca_{2.07}V_2O_{5.39}$ which may be the focal

281 calcium vanadate ($Ca_2V_2O_7$) as reported in the literature [6]. It is possible that not all oxides are

282 oxygen-saturated, which would cause too much oxygen has been excluded and lead to less oxygen

283 in $Ca_{2.07}V_2O_{5.39}$ than that in $Ca_2V_2O_7$. As shown in Fig. 8(d), the generated compounds on the CaO

284 surface and near the V-slag/CaO interface have no visible appearance, and the chemical formula is

285 calculated as $Ca_{4.14}V_2O_{9.45}$. The chemical formula can be split as $Ca_2V_2O_7 \cdot Ca_{2.14}O_{2.45}$ or

286 $Ca_3V_2O_8 \cdot Ca_{1.14}O_{1.45}$, which indicates the compounds consist of $Ca_2V_2O_7$ and CaO or $Ca_3V_2O_8$ and

14

287   CaO or the mixture of $Ca_2V_2O_7$, $Ca_3V_2O_8$ and CaO. This conclusion is consistent with the report

288   [34] that if the temperature is higher than 1023 K and the content of CaO is sufficient, $Ca_2V_2O_7$ and

289 $Ca_3V_2O_8$ may be generated during roasting the V-slag.

290
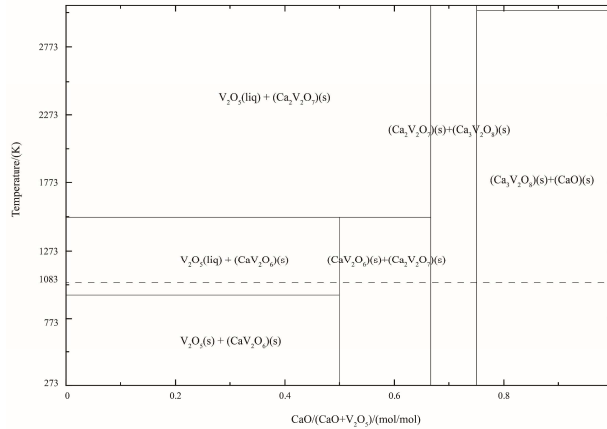
291

292   **Fig. 7.** Phase diagram of the V_2O_5-CaO system calculated by FactSage using the Phase Diagram

293   module.

294

295

296   **Fig. 8.** Microscopic characteristics and EDS spectra of the generated compounds at different

297   locations on the diffusion surface after annealing at 1083 K in the air for 75 minutes.

298

299   The cross-sectional views of the diffusion interface annealed at 1083 K in the air for 75 minutes

are shown in Fig. 9(a), the crystal structures of the generated phases at the region 9-1 and region 9-

2 are characterized by XRD, and the results are shown in Fig. 9(b). According to Fig. 9(b), the

characteristic peaks of $Ca_3V_2O_8$ (JCPDS, 00-039-0090) and $Ca_2V_2O_7$ (JCPDS, 00-028-0836) are

observed in the region 9-1, which verifies the EDS analysis in Fig. 8(c) and Fig. 8(d): the main

generated compounds around the V-slag/CaO interface are $Ca_3V_2O_8$ and $Ca_2V_2O_7$. The diffraction

peaks marked by 4,5 and 6 can be indexed to Fe_2O_3 (JCPDS, 01-089-0597) or $Fe_{1.8966}Mg_{0.1551}O_3$

(JCPDS, 01-070-2674) or Fe_9TiO_{15} (JCPDS, 00-054-1267). The characteristic peaks of Mn_2O_3

(JCPDS, 03-065-7467) are presented in the region 9-2, which verifies the EDS analysis in Fig. 8(b):

Mn^{2+} is oxidized into Mn_2O_3 at the V-slag surface where the diffused Ca has not reached. Besides,

the diffraction peaks of $CaMn_7O_{12}$ (JCPDS, 01-084-0191) are shown in the region 9-2, and it

suggests that some Mn_2O_3 react with CaO and generate $CaMn_7O_{12}$. The diffraction peaks of SiO_2

(JCPDS, 01-079-1912) appears in the region 9-2, which is consistent with the results reported in the

literature [32]. It should be noted that CaO (JCPDS, 01-070-4068) also appears in the region 9-2,

which may be caused by the limitations of the analyzing equipment. When the 2-theta is 90°, the

area of the scanning region (red borders in Fig. 9(a)) is 500 µm × 500 µm. When the 2-theta is less

than 90°, the scanning area is greater than 500 µm × 500 µm, and the CaO surface is scanned.
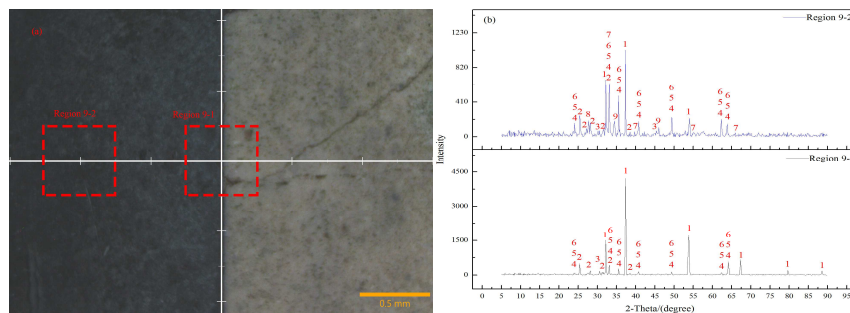
**Fig. 9.** The cross-sectional views captured by SmartLab (a) and the XRD patterns of the generated

16

320 phases at different locations on the diffusion surface (b). 1-CaO; 2- $Ca_3V_2O_8$; 3- $Ca_2V_2O_7$; 4-Fe_2O_3;

321 5-$Fe_{1.8966}Mg_{0.1551}O_3$; 6-$Fe_9TiO_{15}$; 7-$Mn_2O_3$; 8-$SiO_2$; 9-$CaMn_7O_{12}$.

322

323   Fig. 10 shows the cross-sectional views and the elemental maps of the diffusion interface

324 annealed at 1083 K for 5 minutes in the air. The diffusion boundaries marked as the purple dotted

325 curve and the red dotted curve in Fig. 10(a) were determined by the Ca map in Fig. 10(b) and V map

326 in Fig. 10(h). It can be extracted from the EDS analysis that Fe does not diffuse to the CaO surface.

327 Thus, the original interface between V-slag and CaO can be determined by the Fe map in Fig. 10(e)

328 and marked as the gray dotted curve in Fig. 10(a). It can be seen from the three diffusion boundaries

329 that Ca^{2+} diffuses faster than V^{5+} in the generated compounds. As shown in Fig. 10(a), Fig. 10(c),

330 and Fig. 10(h), the regions (region 10-1, region 10-2, and region 10-3) containing primary Mn are

331 only distributed of little V, which confirms the conclusion obtained from the EDS and XRD analysis

332 that most of Mn is enriched into Mn_2O_3 instead of manganese vanadates. As shown in Fig 10(a),

333 Fig. 10(d), Fig. 10(e), and Fig. 10(f), the phase of region 10-4 mainly consists of Fe and O, it should

334 be Fe_2O_3. The phase of region 10-5 mainly consists of Mg, Fe, and O, and it may be

335 $Fe_{1.8966}Mg_{0.1551}O_3$. The phase of region 10-6 mainly consists of Mg and O, and it should be MgO.

336 As shown in Fig. 10(a), Fig. 10(h), and Fig. 10(i), the region 10-7 and region 10-8 contain Cr but

337 do not contain Ca or V. It indicates that Cr is at a disadvantage compared with V when occupying

338 the original Ca in the V-slag, which is consistent with the conclusion in the literature [34]. As shown

339 in Fig. 10(a), Fig, 10(f), and Fig. 10(j), the phase of region 10-9 mainly consists of Si and O, and it
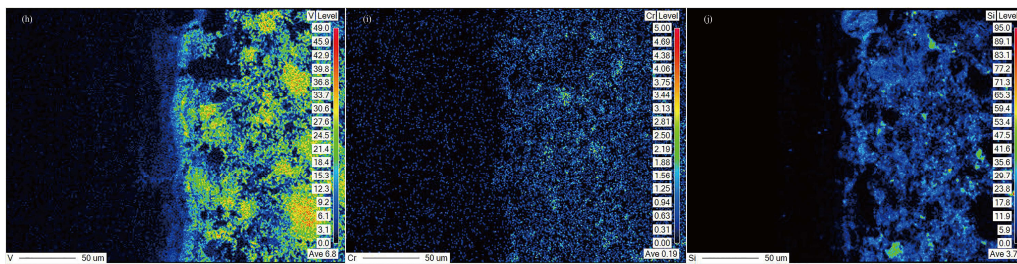
340 may be SiO_2.
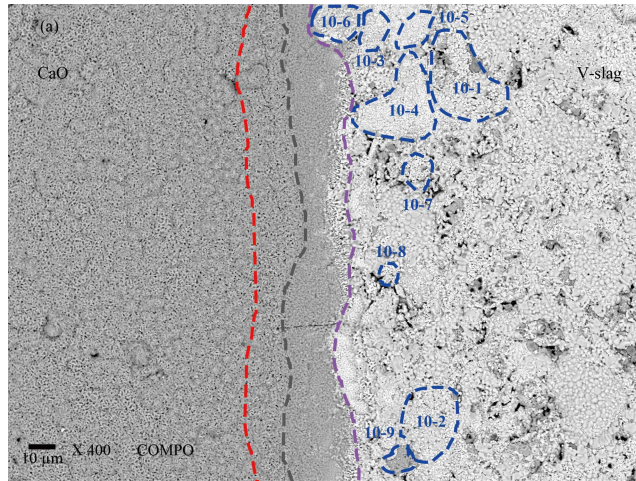
341
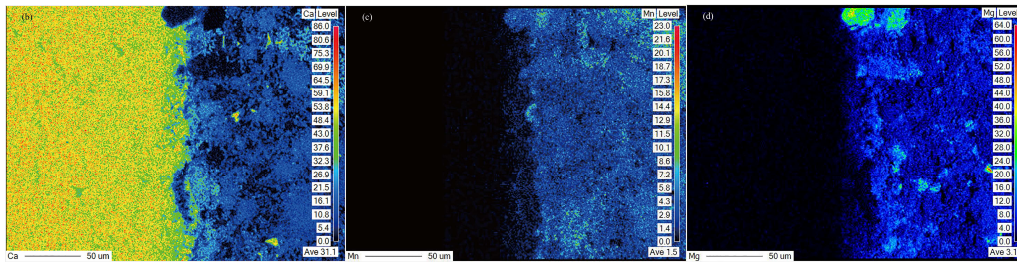
342
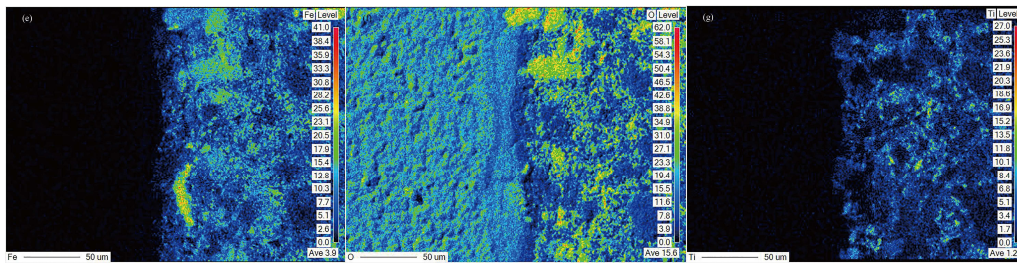
343

344

345 **Fig. 10.** Cross-sectional views and elements maps of the diffusion interface roasted at 1083 K for 5

346 minutes in the air.

347

348 **3.4. Interdiffusion coefficients of Ca^{2+} and V^{5+} in the calcium vanadates**

349

350 The black solid points in Fig. 11(a) are the raw data of the Ca concentration profiles obtained

18

351   by EPMA on the scale line 5-3 in Fig. 5. The red and green histograms in Fig. 11(a) are the

352   concentration differences in Eq. (6) and Eq. (7), respectively. The areas (A_{afh} and A_{efj} in Fig. 3) at a

353   location can be calculated as the sum of the areas of the histograms, i.e., the sum of the concentration

354   difference times the scanning step of 2.5 µm. A_{afh} and A_{efj} are shown in Fig. 11(b), and they are

355   closest at 797.5 µm on the scale line 5-3, which indicates 797.5 µm on the scale line 5-3 is the

356   Matano surface. Subsequently, the new X-axis is established with origin of 797.5 µm on the scale

357   line 5-3. A_{hbgf} in Fig. 3(d) is calculated as the product of the concentration difference in Fig. 11(a)

358   and the coordinate on the X-axis, and the data are shown in Fig. 11(c). Finally, A_{abgf} in the

359   Boltzmann-Matano method can be calculated by Eq. (8) and constructed in Fig. 11(d). The slopes

360   of the raw data of the Ca concentration profiles in Fig. 11(a) are calculated by Eq. (9) and Eq. (10)

361   and plotted in Fig. 11(e). If the Ca concentration curve is monotonic, the slopes should all be positive

362   as the concentration increasing with the increase of the coordinates. However, the calculated results

363   show that the slopes in some intervals are negative. Here, the average of the two positive slopes at

364   both ends of the interval is used to replace the negative slopes in the interval. The interdiffusion

365   coefficients of Ca^{2+} ($D_{\text{Ca2+}}$) as a function of the molar fraction of Ca are calculated by Eq. (11) and

366   presented in Fig. 11(f). The $D_{\text{Ca2+}}$ in the generated compounds are substantially in the orders of

367   magnitudes of 10^{-9} to 10^{-7} cm$^2\cdot$s^{-1}. If the profiles in Fig. 11(a) are strictly increasing with coordinates,

368   the A_{abgf} in Fig. 11(d) and slope in Fig. 11(e) should increase first and then decrease as the coordinate

369   increasing. However, the volatility of the raw data in Fig. 11(a) causes the fluctuations of the A_{abgf}

370   in Fig. 11(d) and the slope in Fig. 11(e), which also affect the calculated $D_{\text{Ca2+}}$ in Fig. 11(f). As usual,

371   the average of the interdiffusion coefficients in a certain concentration interval was proposed to

372   express the diffusion ability [35-37]. In this case, the average of $D_{\text{Ca2+}}$ with the Ca molar fraction of

19

373   0.15-0.86 is calculated as 2.54×10^{-8} cm$^2\cdot$s^{-1}. Besides, the average of D_{Ca2+} calculated by Eq. (11)

374   and the other method [24, 38-40] provided in the literature are listed in Table 2. As given in Table

375   2, the average of D_{Ca2+} calculated by Eq. (11) is in agreement with that calculated by the method

376   reported in the literature [38]. At the same time, the average of D_{Ca2+} in the calcium vanadates is

377   also in the same order of magnitude as that in the $Ca_2Fe_2O_5$ [24]. These results indicate that the

378   method of calculating the interdiffusion coefficient in this paper is reliable. Similarly, the data

379   generated during the calculation of the interdiffusion coefficients using the V concentration profiles

380   are plotted in Fig. 12. The average of the interdiffusion coefficients of V^{5+} with the V molar fraction

381   of 0.001 to 0.43 is 1.96×10^{-8} cm$^2\cdot$s^{-1}. It can be extracted from the calculated results that the diffusion

382   of Ca^{2+} is faster than the diffusion of V^{5+} in the calcium vanadates, and the calcium vanadates are

383   mainly formed on the V-slag surface. Thus, when roasting the V-slag powders with CaO powders,

384   the particle size of the V-slag should be greater than that of CaO.

385   **Table 2**

386   Interdiffusion coefficients of Ca^{2+} calculated in the present work and the literature [24,38]
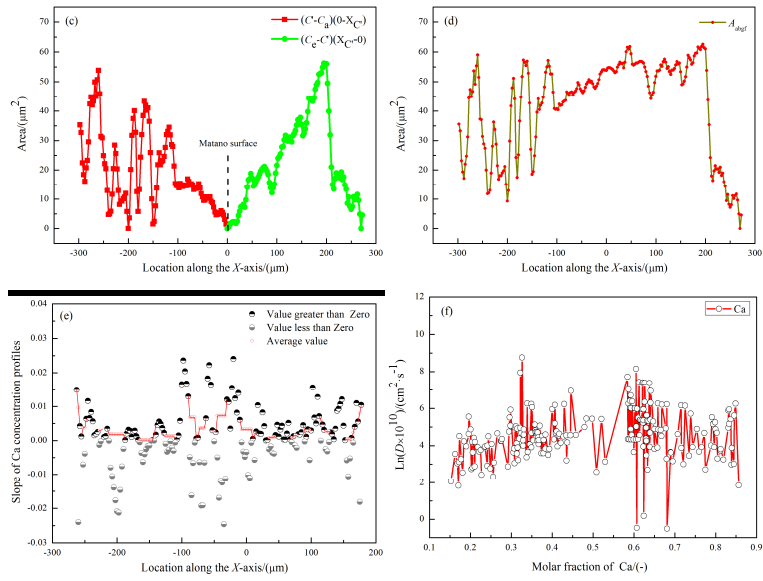
Condition	System	Profiles	Method	Medium	$D_{average}$
1083 K	V-slag/CaO	Fig. 5(f)	Eq. (11)	$Ca_2V_2O_7$, $Ca_3V_2O_8$	2.54×10^{-8} cm$^2\cdot$s^{-1}
1083 K	V-slag/CaO	Fig. 5(f)	Reference [38]	$Ca_2V_2O_7$	5.2×10^{-8} cm$^2\cdot$s^{-1}
1173 K	CaO/FeO	Reference [24]	Reference [24]	$Ca_2Fe_2O_5$	2.0×10^{-8} cm$^2\cdot$s^{-1}

387

388
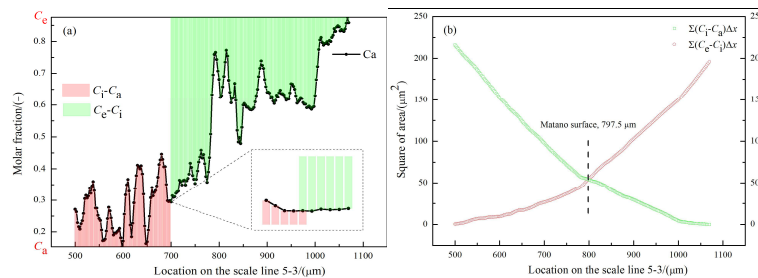
Fig. 11. Calculated data of determining the Matano surface, integral, differential, and the interdiffusion coefficient by the concentration profiles of Ca.
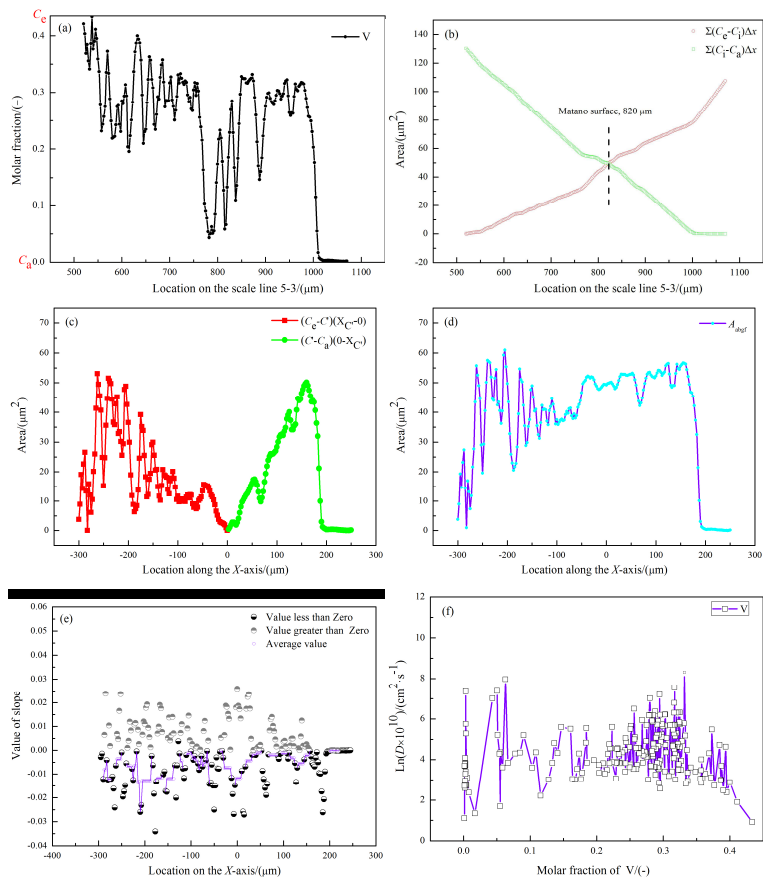

Fig. 12. Calculated data of determining the Matano surface, integral, differential, and the interdiffusion coefficient by the concentration profiles of V.

4. Conclusion

In this paper, the V-slag/CaO diffusion couple was prepared by the vacuum hot-pressing method, and the diffusion experiment was carried out at 1083 K in the air in the muffle furnace. Although the V-slag/CaO diffusion couple can be assembled by the method in this paper, it will start cracking after being stored in a vacuum oven for 1-2 weeks. Therefore, the key to study the diffusion couple containing CaO is to prepare the diffusion couple that will not crack at high temperatures and not deliquesce at low temperatures. Also, the concentration profiles on the V-slag surface are too fluctuant to directly apply in the Boltzmann-Matano method to calculate the interdiffusion coefficient. In this paper, a new method is proposed to determine the Matano surface and calculate the interdiffusion coefficients without smoothing the concentration profiles. According to the result of this paper and related literature, the following conclusions can be used as a reference for the readers.

1. The diffusion thickness of the calcium vanadates is generally proportional to the square root of the roasting time.

2. At the V-slag surface where the diffused Ca has not reached, Fe and Mn are mainly enriched in the corresponding oxides after decomposing from the spinels. The low-valent V is oxidized and reacted with the original Ca in the V-slag to form $Ca_2V_2O_7$. Cr is at a disadvantage of occupying the original Ca in the V-slag comparing with V.

3. At the V-slag surface where the diffused Ca is already reached, the main generated phase is $Ca_2V_2O_7$.

4. At the CaO surface, the main generated phases may be the combination of $Ca_2V_2O_7$ and $Ca_3V_2O_8$.

422   5. The diffusion coefficient of Ca^{2+} in calcium vanadates is greater than that of V^{5+}, which

423   indicates that calcium vanadates are mainly formed on the V-slag surface. Thus, the size of the V-

424   slag particle should be larger than that of CaO particle in the practice roasting.

425

430

431   **Reference**

432   [1] H.Y. Li, H.X. Fang, K. Wang, W. Zhou, Z. Yang, X.M. Yan, W.S. Ge, Q.W. Li, B. Xie,

433   Asynchronous extraction of vanadium and chromium from vanadium slag by stepwise

434   sodium roasting-water leaching, Hydrometallurgy 156 (2015) 124-135.

435   https://doi.org/10.1016/j.hydromet.2015.06.003

436   [2] W.C. Song, K. Li, Q. Zheng, H. Li, A novel process of vanadium extraction from molten

437   vanadium bearing slag, Waste Biomass Valori. 5(3) (2014) 327-332.

438   https://doi.org/10.1007/s12649-013-9286-z

439   [3] A.J. Teng, X.X. Xue, A novel roasting process to extract vanadium and chromium from high

440   chromium vanadium slag using a $NaOH-NaNO_3$ binary system, J. Hazardous Mater. 379

441   (2019). https://doi.org/10.1016/j.jhazmat.2019.120805

442   [4] Y.L. Ji, S.B. Shen, J.H. Liu, Y. Xue, Cleaner and effective process for extracting vanadium

443   from vanadium slag by using an innovative three-phase roasting reaction, J. Clean. Prod. 149

444   (2017) 1068-1078. https://doi.org/10.1016/j.jclepro.2017.02.177

445   [5] E.I.L. Silva, A. Shimizu, H. Matsunami, Salt pollution in a Japanese stream and its effects on

446   water chemistry and epilithic algal chlorophyll-a, Hydrobiologia 437(1-3) (2000) 139-148.

447   https://doi.org/10.1023/a:1026598723329

448   [6] J.H. Zhang, W. Zhang, L. Zhang, S.Q. Gu, Mechanism of vanadium slag roasting with calcium

449   oxide, Int. J. Miner. Process. 138 (2015) 20-29. https://doi.org/10.1016/j.minpro.2015.03.007

450   [7] P. Cao, X.L. Yang, Y. Peng, Z.B. Fu, L. Chen, Research on the mechanism of producing

451   calcium vanadate, Advanced Materials Research 581-582 (2012) 996-1001. https://doi.org/

452   10.4028/www.scientific.net/AMR.581-582.996

453   [8] J.H. Zhang, W. Zhang, Z.L. Xue, Oxidation kinetics of vanadium slag roasting in the presence

454   of calcium oxide, Min. Proc. Ext. Met. Rev. 38(5) (2017) 265-273.

455   https://doi.org/10.1080/08827508.2017.1289197

456   [9] C.J. Li, Z.J. Yuan, R. Guo, W.D. Xuan, Z.M. Ren, Y.B. Zhong, X. Li, H. Wang, Q.L. Wang,

457   Reaction diffusion in Ni-Al diffusion couples in steady magnetic fields, J. Alloy. Comp. 641

458   (2015) 7-13. https://doi.org/10.1016/j.jallcom.2015.04.061

459   [10] Z.S Ren, X.J. Hu, X.X. Xue, K.C. Chou, Solid state reaction studies in Fe_3O_4-TiO_2 system by

460   diffusion couple method, J. Alloy. Comp. 580 (2013) 182-186.

461   https://doi.org/10.1016/j.jallcom.2013.05.114

462   [11] Y. Zhou, Q.Wang, D.L.Sun, X.L.Han, Co-effect of heat and direct current on growth of

463   intermetallic layers at the interface of Ti-Ni diffusion couples, J. Alloy. Comp. 509 (2011)

464   1201-1205. https://doi.org/10.1016/j.jallcom.2010.09.182

465   [12] I.B. Bashir, Mechanisms of densification during the hot pressing of calcium oxide and

466   synthetic doloma, Material Science & Engineering 61(1) (1983) 51-57.

467   https://doi.org/10.1016/0025-5416(83)90125-8

468   [13] M. Peiteado, A.C. Caballero, D. Makovec, Diffusion and reactivity of $ZnO\text{-}MnO_x$ system, J.

469   Solid State Chem. 180(9) (2007) 2459-2464. https://doi.org/10.1016/j.jssc.2007.07.001

470   [14] K.P. Chao, P. Wang, Y.T. Wang, Diffusion and solubility coefficients determined by

471   permeation and immersion experiments for organic solvents in HDPE geomembrane, J.

472   Hazardous Mater. 142 (2007) 227-235. https://doi.org/10.1016/j.jhazmat.2006.08.022

473   [15] C. Matano, On the relation between the diffusion-coefficients and concentrations of solid

474   metals (the nickel-copper system), Jpn. J. Phys. 8 (1993), 109-113.

475   [16] A. Fick, Ueber diffusion, Ann. Phys. 170 (1855) 59-86.

476   https://doi.org/10.1002/andp.18551700105

477   [17] L. Boltzmann, Zur Integration der diffusionsgleichung bei variabeln diffusions-coefficienten,

478   Ann. Phys. 289 (1894) 959-964. https://doi.org/10.1002/andp.18942891315

479   [18] P.J. Tumidajski, G.W. Chan, R.F. Feldman, G. Strathdee, A Boltzmann-Matano analysis of

480   chloride diffusion, Cement Concrete Res. 25(7) (1995) 1556-1566.

481   https://doi.org/10.1016/0008-8846(95)00149-7

482   [19] M.A. Dayananda, Determination of eigenvalues, eigenvectors, and interdiffusion coefficients

483   in ternary diffusion from diffusional constraints at the Matano plane, Acta Mater. 129 (2017)

484   474-481. https://doi.org/10.1016/j.actamat.2017.03.012

485   [20] M. Appel, Solution for Fick's 2nd law with variable diffusivity in a multi-phase system, Scr.

486   Metall. 2(4) (1967) 217-221. https://doi.org/10.1016/0036-9748(68)90231-7

487   [21] C. Wagner, The evaluation of data obtained with diffusion couples of binary single-phase and

488   multiphase systems, Acta Metall. 17(2) (1969) 99-107. https://doi.org/10.1016/0001-

489   6160(69)90131-X

490   [22] C. Heiligers, C.J. Pretorius, J.H. Neethling, Interdiffusion of hafnium carbide and titanium

491   carbide during hot-pressing, Int. J. Refract. Met. H. 31 (2012) 51-55.

492   https://doi.org/10.1016/j.ijrmhm.2011.09.005

493   [23] H.R Yue, X.X Xue, China Patent, No.CN110263292A (2019).

494   [24] H. Fukuyama, K. Hossain, K. Nagata, Solid-state reaction kinetics of the system CaO-FeO,

495   Metall. Mater. Trans. B 33(2) (2002) 257-264. https://doi.org/10.1007/s11663-002-0010-9

496   [25] W.W. Sun, H. Ehteshami, P.R.C. Kent, P.A. Korzhavyi, Self-diffusion of Ti interstitial based

497   point defects and complexes in TiC, Acta Mater. 165 (2019) 381-387.

498   https://doi.org/10.1016/j.actamat.2018.11.056

499   [26] X.W. Zhou, R.E. Jones, J. Gruber, Molecular dynamics simulations of substitutional

500   diffusion, Comp. Mater. Sci. 128 (2017) 331-336.

501   https://doi.org/10.1016/j.commatsci.2016.11.047

502   [27] Z.P. Lin, L.L. Bai, X. Zhang, H.F. Dong, F.G. Wu, Na-vacancies-induced magnetism in

503   Na_xMnO_2, J. Magn. Magn. Mater. 468 (2018) 164-167.

504   https://doi.org/10.1016/j.jmmm.2018.08.009

505   [28] K.N. Goswami, A. Mottura, A kinetic monte carlo study of vacancy diffusion in non-dilute

506   Ni-Re alloys, Mat. Sci. Eng. A-Struct. 743 (2019) 265-273.

507   https://doi.org/10.1016/j.msea.2018.11.064

508   [29] Z.S. Mi, L. Chen, C.M. Shi, Y. Ma, D.C. Wang, X.L. Li, H.M. Liu, L.J. Qiao, The effects of

509   strain and vacancy defects on the electronic structure of Cr_2O_3, Comp. Mater. Sci. 144 (2018)

510   64-69. https://doi.org/10.1016/j.commatsci.2017.12.012

511   [30] K.J. Relmasira, A.Yu. Leonov, P.I. Malenko, Application of molecular dynamics method for

512   simulation of the process of increasing the diffusion mobility, Procedia Engineering 206

513   (2017) 636-641. https://doi.org/10.1016/j.proeng.2017.10.529

514   [31] S.A. Kislenko, M.S. Vlaskin, A.Z. Zhuk, Diffusion of cation impurities by vacancy

515   mechanism in α-Al_2O_3: Effect of cation size and valence, Solid State Ionics 293 (2016) 1-6.

516   https://doi.org/10.1016/j.ssi.2016.05.021

517   [32] X.F. Zhang, F.G. Liu, X.X. Xue, T. Jiang, Effects of microwave and conventional blank

518   roasting on oxidation behavior, microstructure and surface morphology of vanadium slag

519   with high chromium content, J. Alloy. Compd. 686 (2016) 356-365.

520   https://doi.org/10.1016/j.jallcom.2016.06.038

521   [33] X.S. Li, B. Xie, Extraction of vanadium from high calcium vanadium slag using direct

522   roasting and soda leaching, Int. J. Min. Met. Mater. 19(7) (2012) 595-601.

523   https://doi.org/10.1007/s12613-012-0600-8

524   [34] T. Jiang, J. Wen, M. Zhou, X.X Xue, Phase evolutions, microstructure and reaction

525   mechanism during calcification roasting of high chromium vanadium slag, J. Alloy. Compd.

526   742 (2018), 402-412. https://doi.org/10.1016/j.jallcom.2018.01.201

527   [35] L.R. Ram-Mohan, M.A. Dayananda, A transfer matrix method for the calculation of

528   concentrations and fluxes in multicomponent diffusion couples, Acta Mater. 54(9) (2006)

529   2325-2334. https://doi.org/10.1016/j.actamat.2006.01.021

530   [36] P. Zhang, T. Debroy, S. Seetharaman, Interdiffusion in the MgO-Al_2O_3 spinel with or without

531   some dopants, Metall. Mater. Trans. A 27(8) (1996) 2105-2114.

532   https://doi.org/10.1007/BF02651865

533   [37] Y. Yuan, Y.Y. Guan, D.J. Li, N. Moelans, Investigation of diffusion behavior in Cu-Sn solid

534   state diffusion couples, J. Alloy. Comp. 661 (2016) 282-293.

535   https://doi.org/10.1016/j.jallcom.2015.11.214

536   [38] K. Kawamura, A. Saiki, T. Maruyama, K. Nagata, Diffusion coefficient of yttrium ion in

537    $YCrO_3$, J. Electrochem. Soc. 142(9) (1995), 3073-3077. https://10.1149/1.2048690

538   [39] C. Wagner, Investigations on silver sulfide, J. Chem. Phys. 21(10) (1953) 1819-1827.

539   https://doi.org/10.1063/1.1698670

540   [40] T. Maruyama, K. Kawamura, A. Saiki, K. Nagata, Thermodynamics and diffusivity of yttrium

541   in yttrium chromite ($YCrO_3$), Key. Eng. Mater. 111-112 (1995) 303-320.

542   https://doi.org/10.4028/www.scientific.net/kem.111-112.30

543

544

545

546

547

548

549

550

551

552

553

554

555

556   Appendix

557   The meaning of the symbols are lisetd in Table A1.

558

559

Table A1.   Descriptions of the mainly symbols

S	Surface
$S(\mathrm{xz})$	Surface parallel to the x-axis and z-axis
x	Location on the x-axis
x_a	Location of initial concentration
x_e	Location of initial concentration
x_m	Location of Matano surface
X	Location on the X-axis
X'	Location at a particular concentration
C	Concentration
C_a	Initial concentration
C_e	Initial concentration
C_m	Concentration of Matano surface
C'	Concentration at a particular location
$C_{X'-2\Delta X}$	Concentration at $X'-2\Delta X$
$C_{X'-\Delta X}$	Concentration at $X'-\Delta X$
$C_{X'+\Delta X}$	Concentration at $X'+\Delta X$
$C_{X'+2\Delta X}$	Concentration at $X'+2\Delta X$
A	Area
A_{abgf}	Area enclosed by points a, b, g, and f
A_{abm}	Area enclosed by points a, b, and m
A_{dem}	Area enclosed by points d, e, and m
A_{afh}	Area enclosed by points a, f, and h
A_{efj}	Area enclosed by points e, f, and j
A_{hbgf}	Area enclosed by points h, b, g, and f
D	Interdiffusion coefficient
$D_{average}$	Average of interdiffusion coefficient
k	Slope
L_0	Diffusion thickness before roasting
L_x	Diffusion thickness after roasting on the x-axis
t	Time

560

561   Relative error of the calculated interdiffusion coefficient (σ_D/D).

562   The following Eq.(A1) is deduced from the logarithm of the Boltzmann-Matano formula. According

563   to Eq. (A2) and the propagation of error. The relative error of D can be expressed by the relative

564 errors of A and k in Eq. (A3) and Eq. (A4), where the relative error of time is assumed to be zero.

565 According to Eq. (8) and the propagation of error, Eq. (A5) and Eq. (A6) are proposed to calculate

566 the relative error of A. In the sight of Eq. (9) and Eq. (10), the relative error of k can be described

567 by Eq. (A7) and Eq. (A8). Finally, the relative error of D can be calculated as the function of the

568 relative error of C (0.01) as given in Eq. (A9). The relative errors of D at different concentrations

569 are constructed in Fig. A1. In Fig. A1, the relative errors increase sharply as the concentrations

570 closing to the initial concentrations. When the concentrations reach the initial concentrations

571 gradually, the concertation gradient gradually decreases to zero, which lead to the sharply increasing

572 of the relative errors in Eq. (A9). The relationship between the relative error and concentration

573 reflects the limitation of the calculating method in the present work, that is, the calculated

574 interdiffusion coefficients closed to the initial concentrations may have large relative errors.

575
$$LnD = Ln(-\frac{1}{2t}\frac{A}{k}) \tag{A1}$$

576
$$\frac{\sigma_D}{D} \approx \frac{dD}{D} = \mathrm{d}LnD \tag{A2}$$

577
$$\frac{\sigma_D}{D} = \left|-\frac{1}{2t}\frac{A}{k}\right|\left(\left|-\frac{1}{2t}\frac{1}{k}\right|\sigma_A + \left|\frac{A}{2t}\frac{1}{k^2}\right|\sigma_k\right) \tag{A3}$$

578
$$\frac{\sigma_D}{D} = \frac{\sigma_A}{|A|} + \frac{\sigma_k}{|k|} \tag{A4}$$

579
$$\sigma_A = \begin{cases} \Delta X \left|\frac{X_f - X_a}{\Delta X}\right|(\sigma_C + |-1|\sigma_C) + |X_f|(\sigma_C + |-1|\sigma_C), & X < 0 \\ \Delta X \left|\frac{X_e - X_f}{\Delta X}\right|(\sigma_C + |-1|\sigma_C) + |X_f|(\sigma_C + |-1|\sigma_C), & X > 0 \end{cases} \tag{A5}$$

580
$$\sigma_A = \begin{cases} -2X_a\sigma_C, & X < 0 \\ 2X_f\sigma_C, & X > 0 \end{cases} \tag{A6}$$

581 For interior points:

582
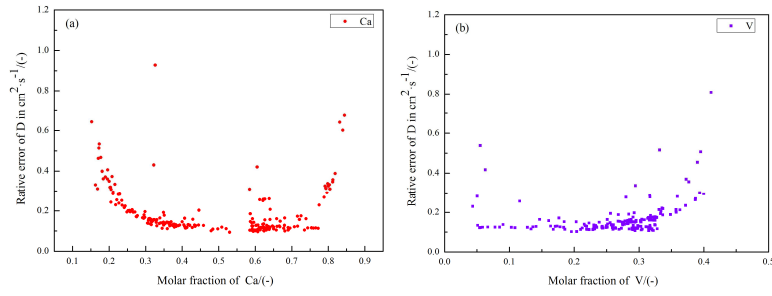$$\sigma_k = \frac{1}{12\Delta X}(\sigma_C + |-8|\sigma_C + 8\sigma_C + |-1|\sigma_C) = \frac{3}{2\Delta X}\sigma_C \tag{A7}$$

583 For end-points:

584
$$\sigma_k = \frac{1}{12\Delta X}(|-25| + 48\sigma_C + |-36|\sigma_C + 16\sigma_C + |-3|\sigma_C) = \frac{32}{3\Delta X}\sigma_C \tag{A8}$$

585

586

$$\frac{\sigma_D}{D} = \begin{cases} \dfrac{-2X_a\sigma_C}{|A|} + \dfrac{\frac{3}{2\Delta X}\sigma_C}{|k|}, & X < 0, \text{interior points} \\[2ex] \dfrac{2X_f\sigma_C}{|A|} + \dfrac{\frac{3}{2\Delta X}\sigma_C}{|k|}, & X > 0, \text{interior points} \\[2ex] \dfrac{-2X_a\sigma_C}{|A|} + \dfrac{\frac{32}{3\Delta X}\sigma_C}{|k|}, & X < 0, \text{end} - \text{points} \\[2ex] \dfrac{2X_f\sigma_C}{|A|} + \dfrac{\frac{32}{3\Delta X}\sigma_C}{|k|}, & X > 0, \text{end} - \text{points} \end{cases} \qquad (A9)$$

587

588 Fig. A1. Relative errors of the calculated Ca^{2+} interdiffusion coefficients and V^{5+} interdiffusion

589 coefficients.